Microfluidic Synthesis of Silver Loaded, pH Sensitive, Nanogels for Enhanced Radiotherapy

By
Kyra Boulding
B.A.Sc., Quest University Canada, 2019

A Thesis Submitted in Partial Fulfilment of the
Requirement for the Degree of

MASTER OF SCIENCE

In the Department of Chemistry

We acknowledge and respect the lək̓ʷəŋən peoples on whose traditional territory the university stands and the Songhees, Esquimalt and W̱SÁNEĆ peoples whose historical relationships with the land continue to this day.

Supervisory Committee

Microfluidic Synthesis of Silver Loaded, pH Sensitive, Nanogels for Enhanced Radiotherapy

By
Kyra Boulding
B.A.Sc., Quest University Canada, 2019

Supervisory committee

Dr. Alexander Brolo, Co-Supervisor
Department of Chemistry

Dr. Karolina Valente, Co-Supervisor
Department of Mechanical Engineering

Dr. Dr. Julian Lum, Committee member
Department of Biochemistry and Microbiology

Abstract

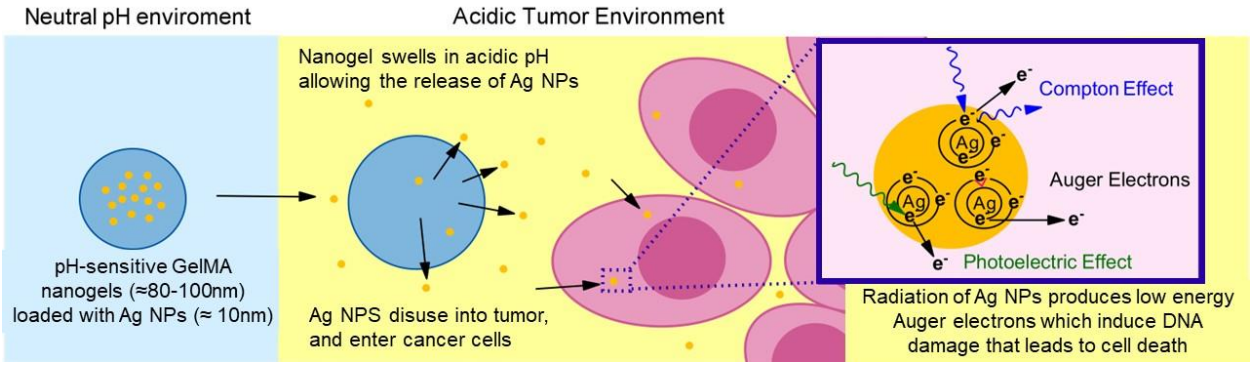

Figure 0.1. Overview of pH-sensitive nanogel for delivery of radiosensitizers to the tumor microenvironment for the enhancement of radiation therapy.

Radiation therapy (RT) is an effective and commonly used course of treatment for cancer. However, RT lacks specificity resulting in sever acute and chronic side effects. Radiosensitizers, like silver nanoparticles (Ag NPs), possess properties that allow for the localized enhancement of RT effects. Nanoscale smart drug delivery systems proved the ability to impose specificity on inherently non-specific treatments. In this work, microfluidics was used to fabricate a pH-sensitive gelatin methacryloy (GelMA) nanogel for the smart delivery of radiosensitizers into the tumor microenvironment. Optimization of synthesis parameters was described, and transmission electron microscopy (TEM) and dynamic light scattering (DLS) were used for characterization. Successful synthesis using a flow focusing microfluidic device produced low-polydispersity (PDI ~0.06), 123 ± 2 nm pH-sensitive GelMA nanogels, loaded with ~ 11 nm Ag NPs. DLS was then used to obtain preliminary evidence of the release of Ag NPs from the nanogels through the appearance, over time, of a second particle population. Additionally, a second synthesis method involving the *in situ* synthesis of Ag NPs during the process of nanogel crosslinking was described. This work provides support for the use of microfluidic devices to produce low-polydispersity nanoscale smart drug delivery systems, with applications in enhancing the efficacy of RT.

Table of Contents

Table of Figures

List of abbreviations

Ag NO_3 - Silver nitrate
Ag NPs - Silver nanoparticles
Au NPs - Gold nanoparticles
DI - Deionized
DLS - Dynamic light scattering
DS - Degree of substitution
EPR - Enhanced permeability and retention
GelMA - Gelatin methacryloyl
HIF - Hypoxia-inducible factors
I-2959 - 2-Hydroxy-4’-(2-hydroxyethoxy)-2-methylpropiophenone
IP -Interstitial Pressure
LAP - Lithium phenyl-2,4,6-trimethylbenzoylphosphinate
MA - methacrylic anhydride
NPs - Nanoparticles
PDI - Polydispersity index
PDMS - Polydimethylsiloxane
RT - Radiation therapy
SDDS - Smart Drug Delivery System
TEM - Transmission electron microscopy
THF - Tetrahydrofuran
TME - Tumor microenvironment
UV - Ultra-violet

Chapter 1 Introduction

Cancer is a traumatic and often lethal diagnosis. The International Agency for Research on Cancer reported that cancer was responsible for nearly 1 in every 6, or 10 million deaths globally in 2020 [1]. For Canadians it is estimated that 43% will be diagnosed with cancer in their lifetime, with 37% not surviving 5 years past their diagnosis [2,3]. The Canadian Cancer Society estimated there were just over 85000 deaths due to cancer in 2022, a jump from the 80,800 deaths in 2017 [2,4]. In addition to a devastating personal and community impact, cancer also comes with a large financial burden. In 2021 cancer related costs to Canadian healthcare were estimated around 26.2 billion, with an additional 4.8 billion in costs being borne by patients and their families [5].

The heterogenous nature of cancer on a tumoral, cellular and genetic level has presented a major challenge for the development of targeted cancer treatments [6–9]. Subsequently, non-targeted and highly cytotoxic treatments such as chemotherapy and radiation therapy have remained popular [10,11]. Though these treatments are effective, the lack of specificity causes off-target toxicity to healthy tissues, resulting in devastating side effects and limiting the doses that can be safely administered [12].

Radiation therapy (RT) is received by more than 50% of cancer patients at some point during their treatment journey [13]. RT is viewed, alongside chemotherapy and surgery, as an effective method of cancer treatment and contributes to around 40% of curative treatments [14]. Due to the non-specific nature of RT, the doses received by patients are limited by both acute and chronic toxicity to surrounding healthy tissues. Acute toxicities that impact rapidly dividing

healthy cell populations, such as hair follicles, are considered reversible, but result in symptoms like hair loss, nausea, and infection [15]. Acute toxicities limit the intensity of the radiation dose that can be administered. Chronic toxicities are considered irreversible damage to tissues that regenerate slowly, such as the liver, kidney, and heart [15]. These toxicities limit the cumulative dose of radiation that can be received within the patient's lifetime. It is then necessary to develop avenues for target treatments that will improve the effectiveness of radiation therapy and reduce the impact on healthy tissues.

Rapidly increasing technical capabilities within the field of nanotechnology provides a unique opportunity to reduce the off target impacts of traditional radiation therapy. Gold and silver nanoparticles have been found to act as radiosensitizers, as their intrinsic properties allow for the impacts of radiation therapy to be enhanced locally [13,16–18]. The development of Smart Drug Delivery Systems (SDDSs), which release the treatment of interest upon the presence of an external stimulus, provide a promising way to lend specificity to delivery of treatment enhancing particles such as radiosensitizers [19,20].

Hydrogels are 3D hydrophilic polymer networks capable of absorbing high volumes of aqueous solution but can maintain their structure through the crosslinking of the polymer chains [21]. Hydrogels are ideal candidates for the creation of SDDSs due to their biocompatibility and highly tunable properties that can be altered to respond to environmental factors such as pH [22–24]. Hydrogel nanoparticles (nanogels) are traditionally synthesized through emulsion processes [25]. However, microfluidic synthesis of nanogels facilitates more control over nanogel size and polydispersity while also allowing for high throughput [25].

This project aims to fabricate a biocompatible and pH activated delivery system for silver nanoparticles using microfluidics. The goal is to facilitate the use of their radiosenziting properties in the improvement of cancer radiation therapy. The first objective of this thesis is to use microfluidics to synthesize nanogels loaded with silver nanoparticles (Ag NPs). The second objective is to characterize loaded nanogels using transmission electron microscopy (TEM) and dynamic light scattering (DLS). Finally, this thesis aims to demonstrate the pH-initiated release of the Ag NPs using DLS.

The first chapter of this work will outline important concepts related to the tumor microenvironment, SDDSs, radiation therapy and radiosensitizers, hydrogels and microfluidic synthesis of nanogels. The second chapter will cover materials, the two different synthesis methods used, and the optimization process. Chapter three will present and discuss the results obtained. The final chapter will cover conclusions and future directions.

1.1. Tumor Microenvironment (TME)

Cancer describes not a single disease but a diverse collection of diseases that possess certain traits, referred to as cancer hallmarks [26]. These hallmarks are acquired by cells through mutations to their DNA, which can be caused either by mistakes during cellular replication, or from exposure to external mutagenic factors. The most notable of these hallmarks is cancer's ability to sustain growth and proliferation signals.

In the growth of healthy cells, proliferation is strictly regulated, both intrinsically and extrinsically, to ensure appropriate function is maintained [27,28]. The Hayflick limit refers to a set

number of cell replications; after which cells undergo senescence, a process which removes them from the replicative cycle [29]. Apoptosis, or programmed cell death, is another mechanism of intrinsic regulation, and is initiated when the cell's DNA undergoes detrimental mutation or damage [28]. Some mutations disrupt/bypass the internal regulatory mechanisms of a cell. In these situations, immune cells function as external regulators and phagocytose or trigger apoptosis in the damaged cells. In cancerous cells the mutations acquired allow them to bypass both the intrinsic and extrinsic regulatory functions, thus achieving unregulated replication [26].

Prolific and sustained growth by cancerous cells alters the physical and chemical characteristics of the tissue within and surrounding the tumor microenvironment (TME). Healthy cells require both lymphatic and circulatory systems within close proximity to provide oxygen and nutrients, and to remove cellular waste [15]. In healthy tissues intrinsic and extrinsic regulatory factors maintain cellular populations that are appropriate for the available vasculature. Lacking regulatory factors, cancer cell populations surpass the capacity of local micro vessels, leading to a hypoxic and nutrient poor TME (**Figure 1.1**) [15,30]. The TME also maintains a reduced pH (7.4 vs 5.8 in some cancers) and increased interstitial pressure (IP), resulting from the lack of oxygen and accumulation of cellular waste [30]. Convection is the driving force behind the movement of molecules and nutrients in healthy tissues, relying on a pressure differential between the blood vessels and the tissue. Diffusion is a comparatively less efficient processes for the movement of molecules within the TEM and is dictated by concentration gradient in addition to the molecule's size, shape, solubility, and tissue interactions [30]. The increased IP in the TME removes the pressure differential, resulting in diffusion being the primary mechanism for molecular movement into

cancerous tissue [30]. This has significant impacts on cancer treatments as it makes the even dispersion of compounds throughout the tumor difficult and size dependent [30].

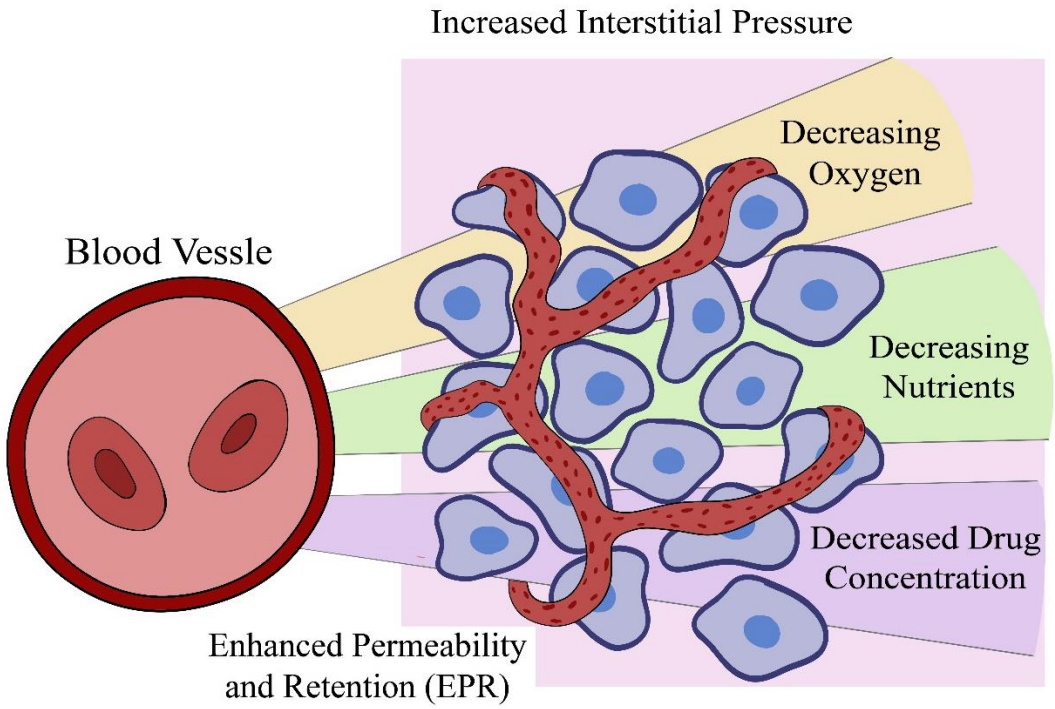

Figure 1.1. Tumor Microenvironment Characteristics.
The characteristics of the Tumor Microenvironment deviate from those of healthy tissue. Accumulation of cellular waste from increasing cell populations results in increased interstitial pressure (IP) and an acidic pH compared to healthy tissue. The increased IP causes movement of nutrients, oxygen and drugs to be diffusion dependent resulting in gradient distributions that decrease with distance from blood vessels. The Enhanced Permeability and Retention (EPR) effect is consequence of tumor blood vessels, whose formation is triggered by the hypoxic environment, being comparatively more porous than vessel found in healthy tissues. This porosity leads to a preferential accumulation of certain sized molecules within the tumor. Figure adapted from; Valente, K. P.; Khetani, S.; Kolahchi, A. R.; Sanati-Nezhad, A.; Suleman, A.; Akbari, M. Microfluidic Technologies for Anticancer Drug Studies. *Drug Discov. Today* **2017**, *22* (11), 1654–1670. [31]

Enhanced Permeability and Retention (EPR) is another influential characteristic of the TME. As cancer cell populations outgrow the local vasculature and a hypoxic environment develops, it leads to the triggering of hypoxia-inducible factors (HIF). HIFs are responsible for initiating the process of new blood vessel formation, or angiogenesis [32]. Blood vessels formed within cancerous tumors are abnormal, notably they have increased porosity compared to blood

vessels in healthy tissues [33]. Leaking of fluids from blood vessels into tumor tissue, because of the increased porosity, partnered with poor lymphatic drainage contributes to higher IP in the tumor [33]. The abnormal porosity of tumor blood vessels also results in particles of a certain size (100 – 200 nm) exiting the blood stream and accumulating preferentially in tumor tissue, known as the EPR effect [34].

The abnormal properties of the TME have a large impact on the effectiveness and delivery of treatments. Anti-cancer treatment often relies on the generation of reactive oxygen species to cause cellular damage and trigger apoptosis, meaning the hypoxic nature of the TME can greatly reduce their efficacy [15]. Increased IP reduces the pressure gradients responsible for drug distribution in healthy tissues, making diffusion of the drug throughout the entirety of the tumor difficult and size dependent [30]. However, the unique properties of the TME can also provide ways to increase specificity of anti-cancer treatments. Creation of treatment molecules in the size range of 100–200 nm can exploit the EPR effect to allow for passive accumulation within the tumor site [34]. The acidic nature of the TME in comparison to healthy tissue can also be utilized as an external trigger for the release of drugs from drug delivery systems [35].

1.2. Smart Drug Delivery Systems (SDDSs)

Advances in nanotechnology have expanded the toolkit of drug delivery beyond traditional methods such as oral, or intravenous injection. The development of micro and nanoscale drug delivery systems has allowed researchers to lend control over location and release of treatments.

SDDSs are a class of drug delivery system that allows for the controlled release of a treatment at a specific site [19]. To classify as a SDDS three steps must occur.

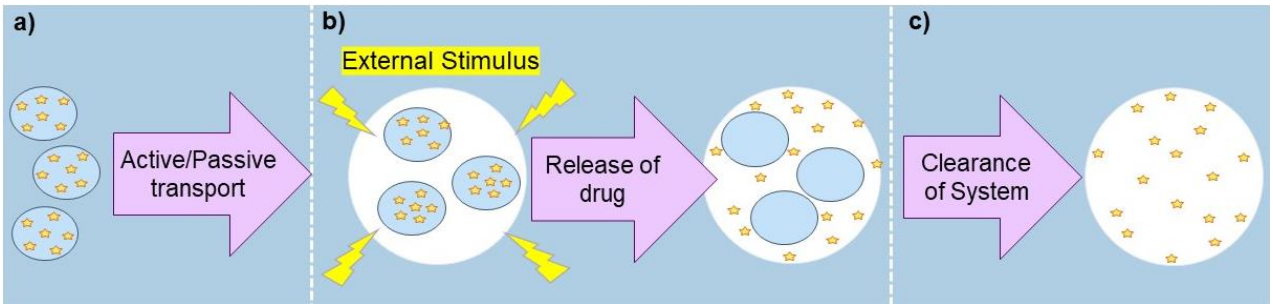

Figure 1.2. Smart Drug Delivery System Scheme.
Smart drug delivery systems are characterized by three distinct events: **a)** Active or passive transport of the drug delivery system to the site of interest. **b)** The release of the drug from the system resulting from an external stimulus. **c)** Removal of the drug delivery system from the body/site of interest.

First, there must be active or passive transport of the system to the target site (**Figure 1.2a**). Passive targeting allows the accumulation of the SDDS in the TME but does not facilitate the uptake of the system by tumor cells [36]. Control over SDDS size to exploit the EPR effect is a common method for passive targeting of tumors [19]. Active targeting involves the uptake of the SDDS by the tumor cell. Active targeting is generally achieved through surface modifications such as the use antibodies, receptor ligands or proteins [36].

Second, an external stimulus present at the target site must trigger the release of the drug from the delivery system (**Figure 1.2b**). Methods such as thermal, ultrasound, and magnetic stimulus have been used, however they present challenges or required activation and knowledge of exact tumor location [37]. The unique properties of the TME, such as pH and hypoxia, can alternatively be leveraged as a stimulus source [19]. The use of TME characteristics as a stimulus source provides the advantage of sustained release of therapeutic agent, as the stimulus is constantly maintained [37].

Third, once the drug has been released the delivery system must be cleared from the site/body (**Figure 1.2c**). Clearance of the SDDS from the target site is important and often occurs via the renal systems or the liver [19]. The size, surface charge, and shape of SDDSs heavily influence their clearance by either system [19]. Alternatively, the SDDS can also be designed to be susceptible to enzyme or environmental degradation in the target site [38].

Delivery of cancer therapeutics is an ideal application for SDDSs as the most commonly used treatments, chemotherapy and RT, are inherently non-specific. Currently, SDDSs have been widely applied to the delivery of anti-cancer therapeutics [19]. SDDSs have been synthesized from a large variety of materials including liposomes, micelles, silica nanoparticles, gold nanoparticles (Au NPs) and nanogles [19,39]. For example, Dong et al. designed a $CaCO_3$ pH-sensitive nanoparticle for the delivery of the commonly used chemotherapeutic agent doxorubicin [40].

1.3. Radiation Therapy

RT attempts to achieve a desired balance that maximizes the exposure of cancerous cells while minimizing the dose received by surrounding healthy tissue. During RT, cancerous tissues are irradiated with ionizing radiation which causes the formation of reactive compounds. Those compounds cause stress and damage to cells, resulting in apoptosis or other forms of cell death [15,41]. Oxygen is a primary electron capturer within cells, and the cytotoxicity caused by RT is predominately due to oxygen free radicals [15]. Radiation can also interact directly with cellular DNA causing double and single strand breaks [14]. The reliance of RT on the generation of oxygen

free radicals to induce cellular stress and damage, means the hypoxic nature of tumors negatively impact the efficacy of RT [14,15,30].

Cells undergoing replication are the most susceptible to damage caused by RT, as those in non-proliferative phases have adequate time to repair cellular damage [15]. Cancer cells continuously undergo replication, due to the failure of regulatory mechanisms [26], making them susceptible to RT. However, as RT is non-specific it also impacts proliferating cells of surrounding healthy tissues such as hair follicles and cells responsible for blood cell production in bone marrow, causing the side effects commonly associated with cancer treatments [15].

1.3.1. Radiosensitizers

The intrinsic properties of radiosensitizers provide a method through which the impact of RT can be locally enhanced. Extensive research has been done on the use of radiosensitizers in RT as it provides a way to increase the dose received by cancer cells without increasing the dose received by healthy cells [16,41–43]. Radiosensitizers rely on the production of low-energy secondary electrons (Auger electrons) due to the photoelectric effect (**Figure 1.3**) [44]. The photo electric effect occurs when an incident photon is absorbed fully by an atom-bound electron, resulting in the ejection of an inner-shell electron [13]. The vacancy in the inner-shell is then filled by an outer-shell electron, causing the release of Auger electrons. Auger electrons travel distances of 1-10 nm making them short range compared to higher energy electrons which can travel micrometers [13]. The majority of DNA damage inflicted by radiosensitizers has been attributed to Auger electrons while long range electrons have been found to have little effect [13]. Radiosensitizer have also been shown to enhance the impact of RT through the creation of reactive oxygen species [18,45].

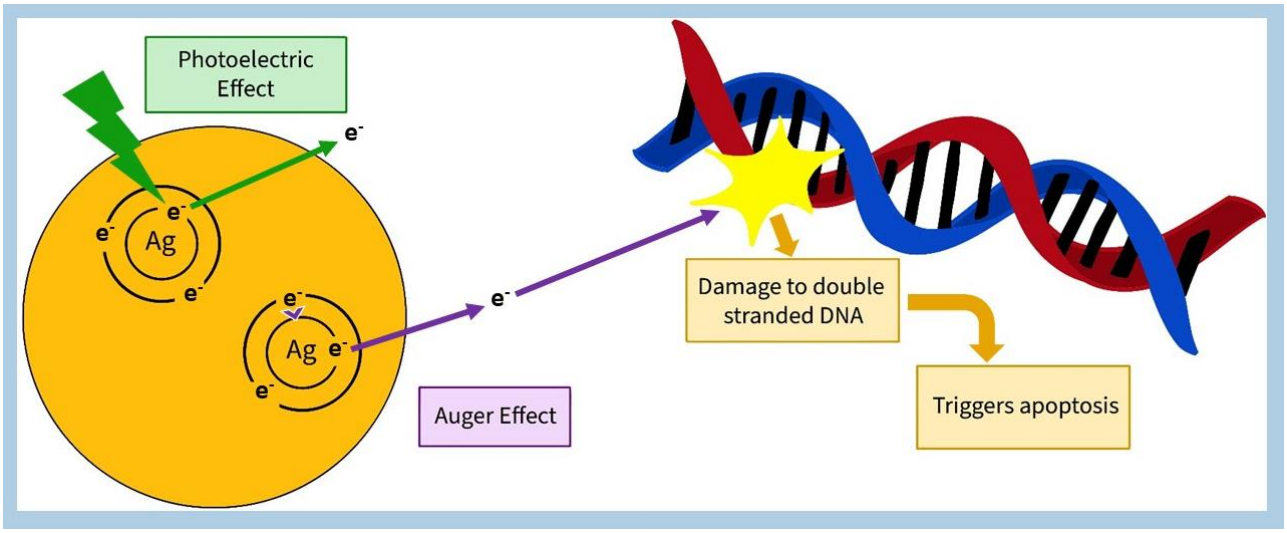

Figure 1.3. Mechanism of Radiosensitization by Ag NPs.
High energy radiation causes the ejection of an electron from an inner orbital of the silver atom via the photoelectric effect. An electron from an outer orbital will then sink to fill the vacancy, causing the ejection of a second, low-energy, Auger electron. Auger electrons cause double stranded DNA damage, which triggers apoptosis in cells.

The probability of a material interacting with irradiation to produce the photoelectric effect is dependent on the energy of the incident photon (E) and the atomic (Z) number of the material, $(E/Z)^3$ [44]. The use of materials with high Z numbers is then crucial for the development of radiosensitizers [13]. Au NPs and Ag NPs have been extensively explored as radio sensitizers due to their high atomic (Z) numbers, 79 and 47 respectively, in comparison to that of soft tissue (7.4) [41,43]. Studies have also demonstrated a size dependence for the radiosensitizing effects of high Z number NPs, with increased NP size being related to reduced performance [18].

The biocompatibility, high Z number, and the preferential accumulation in cancerous tissue exhibited by Au NPs have made them popular as radiosensitizers [45]. Au NPs alone have also been reported to demonstrate anti-cancer and anti-metastatic effects [43]. A 2004 study conducted by Hainfeld et al. injected 1.9 nm Au NPs into the tumors of mice and exposed them to RT [46]. They

demonstrated a one-year survival rate of 86% for mice treated with Au NPs and RT, compared to the 20% survival rate of mice that just received RT [46].

Ag NPs have also garnered interest for use as radiosensitizers due to their relatively high Z number [18]. Liu and colleagues demonstrated the efficacy of Ag NPs as radiosensitizers *in vitro* in a 2013 study[47]. They administered two different concentrations (10 and 20 μg) of ~ 10 nm Ag NPs to glioma-bearing rats, then exposed them to RT. Reported survival time for rats receiving Ag NPs and RT were 100.2 and 98.0 days. In contrast survival times for irradiated controls and rats receiving just Ag NPs (at 10 and 20 μg) were 24.5, 16.1 and 19.4 respectively [47]. A 2018 study by Liu et al. showed that Ag NPs demonstrate an increased radiosensitizing effect in hypoxic conditions compared to normoxic conditions [48]. Given reduced efficiency of RT in hypoxic environments has presented a significant limitation to is use [18,45] , this is a notable characteristic. The improved performance of Ag NPs in hypoxic conditions was in part attributed to Ag NPs inducing higher levels autophagy within cancer cells [48]. Lui and colleagues also compared the efficacy of 15 nm Au NPs and Ag NPs at equal molar and equal mass concentrations both *in vivo* and *in vitro* [43]. Results of the study showed Ag NPs produced higher levels of apoptosis when combined with RT than Au NPs. Increased radiation enhancement by Ag NPs compared to Au NPs was attributed to the increased ability of Ag NPs to induce autophagy within cancerous cell [43].

The use of Au and Ag NPs as radiosensitizers presents a promising solution to increasing the impact of RT doses without increasing the dose received by healthy tissues. However, the properties of nanoparticles are highly dependent on size, surface modification and shape among other factors which has led to ambiguity in the toxicity of Au and Ag NPs [18,45]. This presents a

need for targeting NPs to tumor sites, and to prevent the distribution and uptake in healthy tissues during the process. Loading of radiosensitizers into drug delivery systems such as SDDSs is a viable option for preventing interactions between Au or Ag NPs and the biological environment prior to arriving in the target site.

1.4. Hydrogels

In recent decades the biocompatibility and tunable properties of hydrogels has popularized their use within the biomedical field, with applications in tissue engineering, biosensing and drug delivery [49–54]. Hydrogels have a 3D architecture composed of a network of hydrophilic polymers [21]. The presence of the hydrophilic groups within the main chain of the polymers enables these networks to absorb and retain high volumes of aqueous solutions, a property referred to as 'swelling' [24]. However, the hydrogels can be rendered insoluble in aqueous solution through either chemical or physical crosslinking of the polymer chains [55]. Exposure to light at the wavelengths in the UV (200-400nm) or visible (400-800nm) range, or photopolymerization, is a common mode of crosslinking hydrogels as it offers ease of control over area and time of exposure and requires mild reaction conditions [56]. At their most basic photo-crosslinkable hydrogel systems contain the desired pre-polymer and a photoinitiator; other additional components such as cells [57], nanoparticles [58] or drug molecules [34] can also be added [55]. The synthesis of the pre-polymer and the hydrogel can be tuned to alter the mechanical properties of the hydrogel such as its degradation, pore size, and swelling [23,59,60].

Hydrogels can be made of synthetic (poly (ethylene glycol), poly (vinyl alcohol), etc.), natural (chitosan, cellulose, gelatin, etc.), or semi-synthetic pre-polymers, combinations of these can also be used [61]. Both synthetic and natural hydrogels offer the advantages of biocompatibility, low immunotoxicity and tunable properties [24,55]. Natural hydrogels, however, can be favored for certain applications, due to their variety of functional groups that can facilitate cell adhesion and erosion by enzymes naturally present in cells [38]. The erosion of a hydrogel by enzymes can be advantageous for SDDS applications, where after the release of the desired drug the removal of the system (the hydrogel) from the body is imperative.

1.4.1. Gelatin Methacryloyl (GelMA) Hydrogels

Gelatin methacryloyl (GelMA) hydrogels are a commonly used natural hydrogel, which was first synthesized by Van den Bulcke et.al [62] in 2000. GelMA is composed of gelatin, obtained through the denaturation and hydrolysis of collagen, in which the lysine and hydroxylysine have been substituted with methacrylic anhydride (MA) (**Figure 1.4a**). The methacrylation of gelatin does not alter the arginine-glycine-aspartic acid peptide or the matrix metalloproteinase peptide, which allows GelMA to retain the biocompatibility and enzymatic degradability of gelatin [38]. The degree of substitution (DS) of the carbon double bonds for MA can be controlled by adjusting the pH of the reaction or altering the amount of MA added [23]. The ability to adjust the DS in a GelMA molecule is key, as it dictates the mechanical properties of the hydrogel such as its degradability and ability to absorb water. A 2012 study by Chen et.al. demonstrated that increased DS resulted in more rigid gel with higher durability and smaller pore size [59].

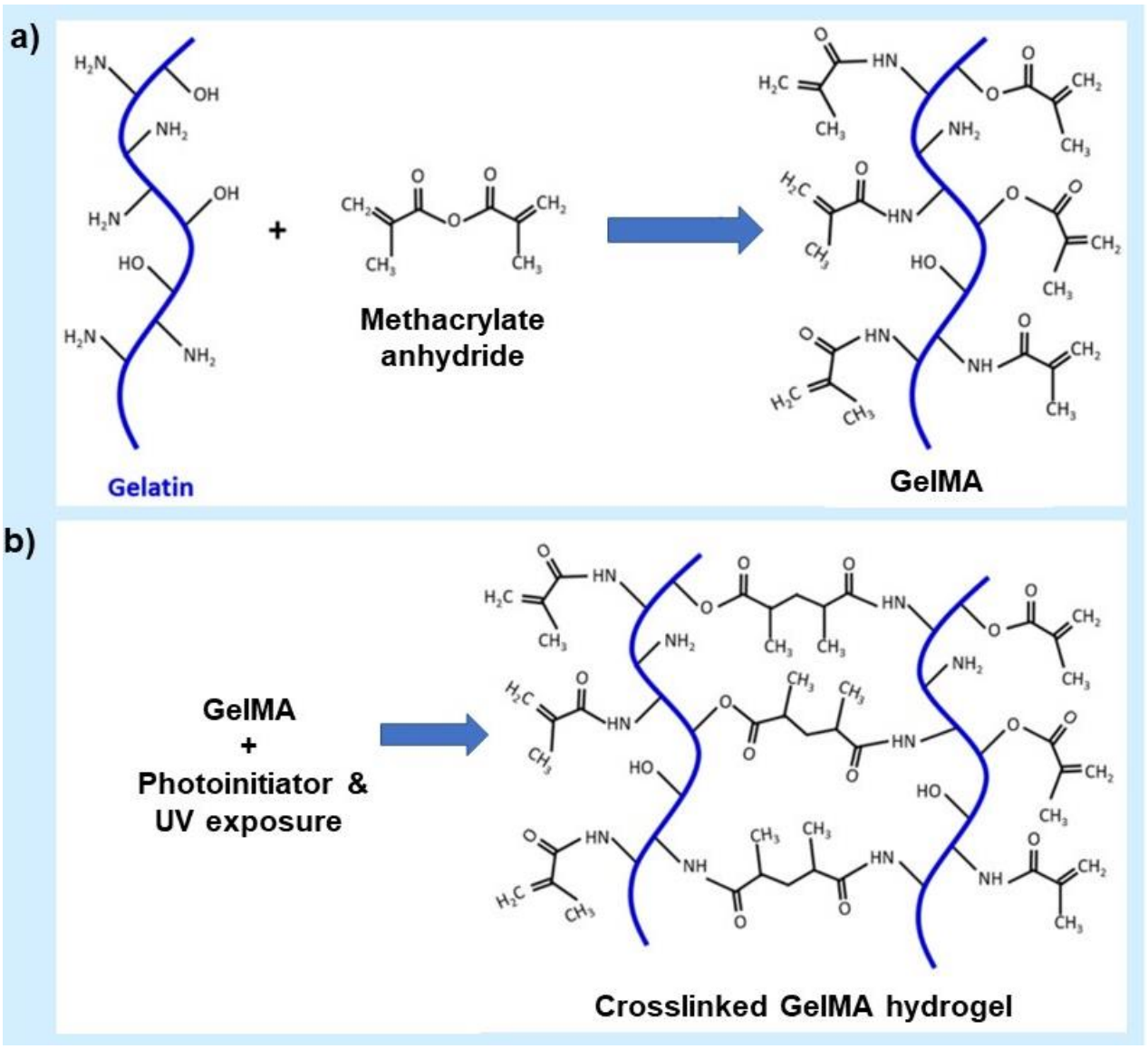

Figure 1.4. Formation and crosslinking of GelMA.

a) The methacrylation of gelatin to form GelMA pre-polymer. **b)** Crosslinking of GelMA pre-polymer to form GelMA hydrogel. Adapted from "Gelatin Methacrylate Hydrogel for Tissue Engineering Application - A Review on Material Modifications." Bupphathong, S. *et al. Pharmaceuticals 2022, Vol. 15, Page 171* **15**, 171 (2022). [63]

In addition to the DS, Van Vlierberghe et.al. examined the impact of the concentration of GelMA polymer on the hydrogel pore size. Their study found an inverse relationship between the pore size and the GelMA concentration [64]. The mechanical properties of GelMA hydrogels can also be tuned by adjusting the type of photoinitiator and crosslinking parameters [60]. GelMA and GelMA-hybrid

hydrogels have been used extensively in the field of tissue engineering and cell encapsulation due to their ease of tunability, biocompatibility, the retained gelatin functions of enzyme degradability and cell adhesion [23,51,59,62,65]. A 2012 study by Chen et. al. used GelMA as a 3D scaffold for co-cultures of blood-derived endothelial colony forming cells and bone-derived mesenchymal stem cells, resulting in the *in vitro* and *in vivo* formation of functional capillary-like networks [59]. That work demonstrated the use of GelMA hydrogels in the growth of complex tissues.

1.4.2. Photoinitiators

The choice of photoinitiator used to induce the photopolymerization of GelMA hydrogels is crucial as they differ in cytotoxicity, water solubility, absorption spectrum, molar extinction coefficient, ability to produce free radicals and stability [66]. Radical photoinitiators are most widely used for biomedical applications. They present higher biocompatibility compared to cationic photoinitiators, which produce H^+ (aq) that can negatively impact cells [66,67]. 2-Hydroxy-4'-(2-hydroxyethoxy)-2-methylpropiophenone (I-2959) has been one of the most broadly used photoinitiators for UV polymerization of hydrogels in biomedical applications [66,68,69]. I-2959 is a Type-I radical photoinitiator, also known as a cleavable photoinitiator [66]. Cleavable photoinitiators instigate crosslinking with two radicals produced when the exposure to radiation causes the photoinitiator to undergo cleavage [69]. The wide use of I-2959 in tissue engineering is due to its low cytotoxicity and moderate water solubility (< 2%wt in ambient conditions) [70–72]. However, several studies have since suggested the cytotoxicity of I-2959 varies considerably and is impacted by several factors [70,73–75]. In a 2005 study, Williams et.al. tested the cytotoxicity of I-2959 at concentrations of 0%, 0.03%, 0.05% and 0.1% (w/v) across six different cell types. It was found that the cytocompatibility of I-2959 varied both with cell type and concentration of the photoinitiator. The study also showed increased toxicity with increased concentration of I-2959

across most cell types, and significant impact on cell survival across all cell types at the concentration of 0.1% (w/v) [70]. A study by Nguyen et.al. in 2019 examined the impact of I-2959 concentration and UV exposure time on the viability of hydrogel encapsulated human osteosarcoma cells (Saos-2). Their findings showed that a concentration of 0.02% (w/v) of I-2959 led to a significant decrease ($p < 0.05$) in cell viability with 1 min of UV exposure vs. 10 min of exposure. That work indicated that length of irradiation impacts I-2959 toxicity. Nguyen and colleagues also found that an increase of I-2959 to 0.1% (w/v) significantly reduced ($p < 0.05$) viability of cell populations overall with the highest viability reduction for cells also exposed to 10 min UV irradiation. I-2959 also has a low molar extinction coefficient (4 M^{-1} cm^{-1}) at 365nm, the commonly used wavelength for crosslinking of hydrogels, which causes decreased reaction efficiency [72,76]. The varied range of cytotoxicity observed for I-2959, it's moderate solubility in water, and its low molar extinction coefficient at 365nm has spurred the search for an alternative photoinitiator [73,74].

Lithium phenyl-2,4,6-trimethylbenzoylphosphinate (LAP) is cleavable photoinitiator that presents an alternative to I-2959 due to its high solubility in water and increased cytocompatibility [66,74]. While I-2959 has a reported solubility limit of less than 2 wt% in water at room temperature [72], LAP has a much higher solubility limit of 8.5 wt% [77]. A 2020 study conducted by Xu et.al. explored cell viability of GelMA encapsulated fibroblasts with varying concentrations of I-2959 or LAP. Xu and colleagues found that while the cell viability for I-2959 and LAP were comparable at low concentrations (0.3%, 0.5% w/v), LAP had much higher overall cell viability at higher concentrations (0.7%, 0.9% w/v). LAP also boasts a higher molar extinction coefficient of 218 M^{-1} cm^{-1} at 365 nm, allowing for a higher initiation rate and a reaction efficiency [72]. In

addition to the DS, Van Vlierberghe et.al. examined the impact of the concentration of GelMA polymer on the hydrogel pore size. Their study found an inverse relationship between the pore size and the GelMA concentration [63]. Increased cell viability at higher concentrations of photoinitiator, higher water solubility and a larger molar extinction coefficient at 365nm have made LAP a favored alternative to I-2959 for photopolymerization of hydrogels for biomedical applications [76].

1.4.3. Nanogels

Nanogels refer to crosslinked, nano-scale hydrogels that are often characterized by spherical shape [25]. Nanogels retain the biocompatibility, tunability, degradability and swelling properties of the hydrogel, while also possessing features of a nanoparticle which make them ideal candidates for drug delivery [25,78–80]. The hydrogel nature of nanogels allows them to be easily modified to be responsive to environmental changes like temperature or pH [78]. Nanogels with pH responsivity have been extensively studied as drug delivery candidates for cancer therapeutics due to the acidic nature of the TME [19,35,78]. A 2017 study by Yang and colleagues synthesized nanogels loaded with the commonly used anti-cancer drug doxorubicin [81]. The nanogels were shown to be stable at the normal body pH (7.4), but in the presence of a mildly acidic environment (pH 5-6) the nanogels degraded causing the release of doxorubicin. Another 2017 study performed by Sahu et al. loaded pH-responsive nanogels with the anti-cancer drug bleomycin to target skin cancers and demonstrated the drug release in the pH range of 5-6 [82].

Emulsion polymerization is a commonly used technique for generation of nanogels [25,83]. This method generates low-polydispersity stable droplets (disperse phase) in a continuous phase. The polymerization is confined to the droplets, and droplet size influences the final size of the nanogels. The formation of nanogels generally follows the process of nucleation, precursor

nanogel growth and finally polymerization [25]. Use of organic droplets containing desired monomers/polymers dispersed in an aqueous solution is generally referred to as direct emulsion. Inverse emulsion refers to the dispersion of aqueous droplets in an organic continuous phase [25]. Reagents used for nanogel synthesis can all be dissolved in the disperse phase, a technique that generally makes use of a photoinitiator to instigate the reaction via radical formation. Alternatively, the dispersed and continuous phases can contain different dissolved monomers. In that approach the continuous phase generally contains an initiator while the disperse phase often has a crosslinker and a catalyst. In emulsion synthesis the stability of droplets formed can be increased by use of a surfactant, allowing for the formation of nanogels < 150 nm [25]. However, emulsification polymerization is limited due to the difficulties in purifying nanogels for biological use, the requirement of large amounts of surfactant and the challenges in scalability [25,83].

1.5. Microfluidics

Microfluidics refers to the use of channels in the range of tens to hundreds of micrometers, for the movement and manipulation of nanoliter and microliter volumes [84]. Microfluidic devices are governed by the laws and mechanisms of mixing within this restricted volume, which differ from the laws and mechanisms present in macroscale mixing devices. In microscale devices viscous forces dominate resulting in the key characteristic of laminar flows, that can't be attained in macroscale devices [84]. Laminar flow is one of two fluid flow regimens and refers to a flow in which all fluids run parallel with no currents that run parallel to the flow direction. In laminar flow the domination of viscous forces results in molecular diffusion dependent mixing of the fluids. The second regimen is turbulent flow which involves the presence of flow vortex and is dictated by

random motion. The Reynolds number (Re) is used to describe the type of flow regimen, with high Re values (> 100) indicating turbulent flow and low Re values (< 100) indicating a laminar flow [84]. The Re is dependent on many parameters including the density, viscosity, and velocity of the fluid as well as the geometry and surface properties of the channels.

In recent decades microfluidic technologies have been extensively used within biomedical fields [31,84]. Use of microfluidics in developments such as organs on a chip have greatly improved the testing of anti-cancer therapeutics through more accurate simulations of tumor environments [31]. Recently, microfluidics has also been used in to synthesize nanogels and nanogel-based drug delivery systems [25,85]. Microfluidic chips are a commonly used microfluid device as they allow for increased control over channel design compared to capillary based devices [86]. Polydimethylsiloxane (PDMS) is a heavily used material for microfluidic chips as it offers optical transparency, flexibility, and low cost [86].

Microfluidic synthesis of nanogels generally makes use of two phases; a solvent phase containing nanogel precursors, and a non-solvent phase which is immiscible. The mixing of the two phases within microfluidic devices results in the formation of particle, through the process of molecular diffusion [84]. A key parameter in the control of nanogel morphology is the mixing time of the two phases, with increased mixing time producing larger particles [84]. Mixing time can be controlled by manipulation of phase flow rates, or length of the channel in which the phases are mixing.

Flow focusing microfluidic devices are a method through which the mixing time of phases can be reduced, resulting in the rapid generation of nanoscale particles [86]. Flow focusing devices

are generally composed of a central channel, containing the solvent phase, that merges at a junction with two lateral channels (non-solvent phase). The junction of these devices then produces a flow composed of a core flow (solvent phase) bordered by a sheath flow (non-solvent phase) on either side [25]. Use of low flow rates for the solvent phase and high rates for the non-solvent phase result in a squeezing of the core flow by the sheath flows, reducing mixing time of the phases [86].

Microfluidic synthesis offers advantages over traditional synthesis methods such as reduced volume of reagents and precise control over particle characteristics [87]. Additionally microfluidic devices offer the potential of scalability. While the batch size of bulk synthesis is limited by increased size dispersity, microfluidics offers scalability through continuous synthesis and the small size of devices allowing for parallel synthesis of man devices simultaneously.

Chapter 2 Particle Fabrication

2.1. Materials

pH sensitive GelMA pre-polymer [88] obtained from VoxCell BioInnovation. Photoinitiator Lithium phenyl-2,4,6-trimethylbenzoylphosphinate (LAP, ≥95%), Span ® 80 (nonionic surfactant), Trichloro(1H, 1H, 2H, 2H-perfluoroctyl)saline (saline), Silver Nitrate ($AgNO_3$, 99%), and Photoinitiator 2-Hydroxy-4’-(2-hydroxyethoxy)-2-methylpropiophenone (I-2959, 98%) were

purchased from Sigma Aldrich. Phosphate Buffer Saline pH 7.4 (PBS) was purchased from Gibco. Hexane (HPLC Grade), and Toluene (Certified ACS) were purchased from Fisher Chemical. NanoXact 10nm Silver Nanospheres – Bare (Citrate) (0.02mg/mL) were purchased from NanoCompSix.

2.2. Equipment

Kd Scientific LEGATO 1111 Dual Syringe Pump, Harvard Apparatus Pump 11 Elite, JEOL JEM-1011 Transmission Electron Microscope, Lecia DM LM microscope, Genie Nano camera, Anton Paar Litesizer 500 Particle Analyzer (semiconductor laser diode / 40mW, 658nm). Support Films, Formvar 200 mesh, Cu (01700-F) and Support Films, Carbon 200 mesh, Cu (01840-F) obtained from Ted Pella Inc. Omega Cuvette for Zeta Potential Measurements obtained from Anton Paar. PerkinElmer Lambda 1050 UV/VIS/NIR Spectrometer. Pre-patterned silicon wafers (76.2 mm diameter, P-type, boron) obtained from Dr. Valente.

2.3. Preparation of Solvent and Nonsolvent Phases

Preparation procedures for both solvent and nonsolvent phases were adapted from the original preparation methods outlined by Dr. Valente [88]. The degree of methacrylation of the GelMA pre-polymers used is reported in mmol of methacrylic groups / 1g of polymer. GelMA pre-polymers used for the loaded nanogel synthesis had degree of methacrylation between 0.1584 and 0.3670 mmol/g as reported by VoxCell BioInnovations.

2.3.1. Preparation of GelMA Solution without Ag NPs (Solvent Phase) (7.5% GelMA polymer : 1% Photoinitiator)

The photoinitiator (LAP) was weighted out (1% w/v) into a glass vial and 1mL PBS pH 7.4 is added. The mixture was then placed in the oven < 60C° until fully dissolved. Once dissolved, the GelMA polymer was added to the solution for a final concentration of 7.5% (w/v). The solution was placed back in the oven < 60C° until GelMA polymer was fully dissolved. The solution was wrapped in tinfoil to protect from light and stored in a bench drawer.

2.3.2. Preparation of GelMA Solution (Solvent Phase) with Ag NPs (7.5% GelMA polymer : 1% Photoinitiator)

The photoinitiator (LAP) was weighted out (1% w/v) into a glass vial, and 1mL 10nm silver nanospheres – Bare (Citrate) (Ag NPs) at a concentration of ~10^{12} particles/mL (as per manufacturer) was added. The solution was placed in an oven < 50 C° until the LAP was fully dissolved. GelMA polymer was weighted out to 7.5% w/v and added to the LAP and Ag NPs mixture, then placed back into the oven < 50 C° until the polymer is fully dissolved. Solution was then removed from the oven, wrapped in tinfoil, and placed in a dark place at room temperature for a minimum of 12 h before use.

2.3.3. Preparation Of Non-Solvent Phase

Non-solvent phase was prepared on the day of the synthesis. 4.5 g of surfactant (Span® 80) was weighted into a glass vial, then 20 mL of toluene was added. The mixture was stirred vigorously by repeated inversion of the glass vial until it appeared homogeneous.

2.4. Flow Focusing Microfluidic Chip Synthesis

The procedure for the synthesis of the nanogels using a microfluidic chip was obtained from Dr. Valente [88]. Silicon wafers patterned via standard SU-8 and photolithography methods were prepared by Dr. Valente (**Figure 2.1a**). The pattern, clearly visible in **Figure 2.1a & b** consisted of two 100µm lateral channels that intersected a 100µm central channel at 150°. Wafers and a tinfoil "boat" containing 20 µL trichloro saline for each wafer were placed in a desiccator under static vacuum seal for ~30 mins. Approximately 20 g of polydimethylsiloxane (PDMS) mixed with curing agent at a 10:1 ratio was poured on to each wafer. The trichloro saline prevented the cured PDMS from sticking to the silicon wafer. Air bubbles were removed from the PDMS by placing it under a vacuum, then releasing the vacuum to degas. The wafers were then placed in a hot plate at ~210 °C for 2 h to cure. The PDMS was removed from the wafer and placed in a petri dish to cool. Once cooled, holes were punched into the inlets to accommodate 0.020 x 0.060" tubing and in the outlet for 0.010 x 0.030" tubing (**Figure 2.1c**).

Glass slides were cleaned with 70% ethanol and allowed to air dry. PDMS was mixed with the same 10:1 ratio and a spin-coater (acceleration 10s, deceleration 10s, spin time 30s, speed 1200 rpm) was used to evenly disperse the PDMS onto the glass slides. Coated slides were then placed on a hot plate to cure at ~ 100 °C for a minimum of 2 h, then allowed to cool down. Coated glass slide and PDMS chips are then washed in baths of soap and deionized water, deionized water and ethanol respectively, then dried fully. A PDMS chip and a coated glass slide were then placed into the plasma cleaner, with the design side of the chip and coated side of the glass slide facing up, for 6 mins. The design side of the PDMS is then pressed firmly onto the coated side of the slide until all are bubbles are removed. The microfluidic chip is then placed on a hot plate at ~110 °C and a

weight was set on top for 15mins, then it was transferred to the oven at ~ 80 °C overnight. The complete chip (**Figure 2.1b**) was removed from oven and tape was placed over the inlet/outlet holes to keep out dirt.

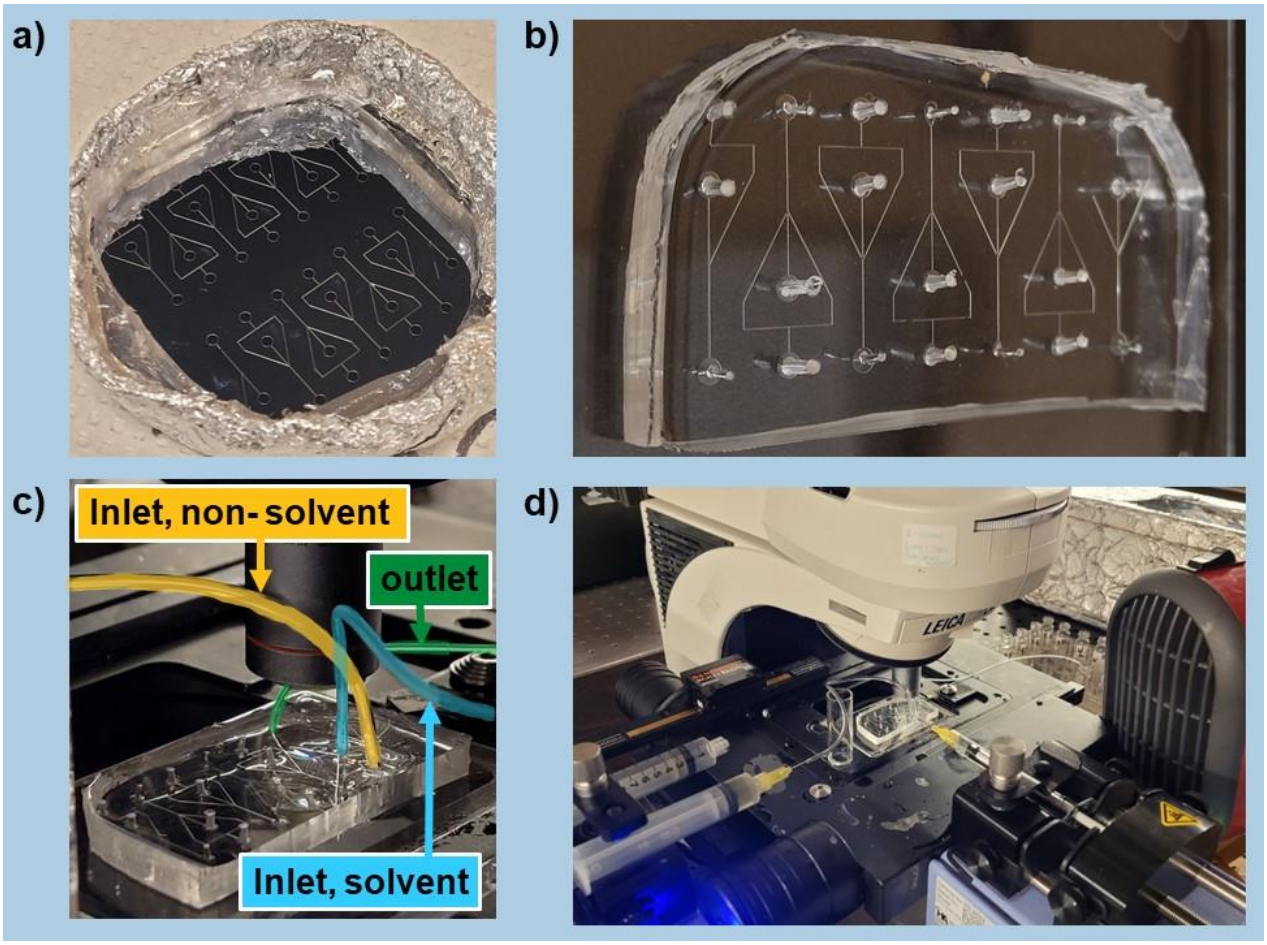

Figure 2.1. Microfluidic-chip Preparation and Set up.
(a) Silicon wafer imprinted via standard photolithography methods, with a flow focusing channel pattern composed of two lateral (non-solvent phase) channels that intersect a central (solvent phase) channel at 150°. All channels are 100 μm. **(b)** Final PDMS microfluidic chip adhered on a glass slide which is spin coated in PDMS, with two large inlets and a small outlet. **(c)** Microfluidic chip set up on stage of Lecia DM LM microscope (5x lens), 0.020 x 0.060" tubing is used for inlets and 0.010 x 0.030" for outlets. **(d)** Full set up for nanogel synthesis; syringe pumps used to dispense solvent and non-solvent phases at constant rates, heater is placed to keep GelMA at a low viscosity, 1.5 mL collection vials used to collect nanogels from the outlet channel.

2.5. Nanogel Fabrication via Microfluidics

A hydrodynamic flow focusing microfluidic chip was used to synthesize GelMA Nanogels (**Figure 2.1b**). The microfluidic chip was set up on the stage of the Lecia DM LM microscope (**Figure 2.1d**) and a Genie Nano camera was used to visualize the solvent and nonsolvent phase streams at the junction of the chip on a computer monitor. It is important to note that while the two phases could be visualized, the nanogels cannot be seen. Instead, the formation of the nanogels is indicated by a blurring of the edges of the solvent phase stream. The nonsolvent phase, composed of Span® 80 and Toluene, was loaded into a 10 mL syringe connected to the chip inlets via tubing (**Figure 2.2**).

A syringe pump was used to inject the nonsolvent phase through the two lateral channels of the chip at a flow rate of 400 µL/min. Span® 80 functions as a surfactant, reducing the interfacial tension between the nonsolvent phase and the aqueous GelMA (solvent phase). The surfactant also stabilizes the nanogels prior to crosslinking, preventing the aggregation and merging of nanogels during collection. The solvent phase, composed of GelMA polymer and PBS pH 7.4 or colloidal Ag NPs, was loaded into a 1 mL syringe connected via tubing to the central channel of the chip. GelMA retains several properties of gelatin, including gelation at room temperature to produce a physically crosslinked hydrogel [23].

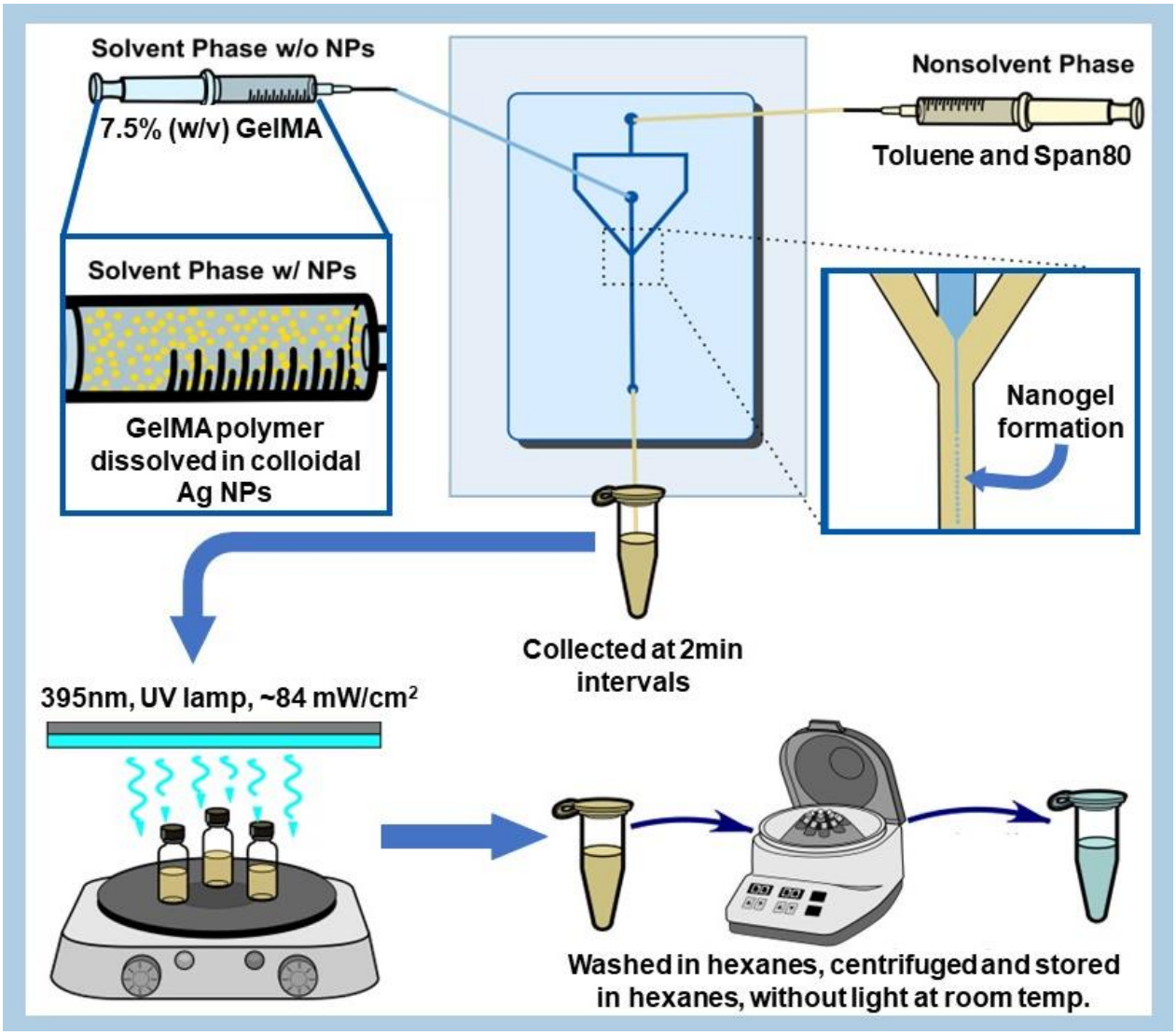

Figure 2.2. Nanogel Synthesis.

The solvent phase is composed of GelMA pre-polymer and the photoinitiator dissolved in colloidal Ag NPs. Toluene and a surfactant (Span80) make up the non-solvent phase. The solvent phase is pumped through the central channel inlet of a flow focusing microfluidic device, while the non-solvent phase is pumped through the lateral inlet channel. The phases meet at the junction, causing jetting of the solvent phase which leads to nanogel formation. Nanogel samples are collected at 2min intervals, then allowed to stabilize overnight without light. Nanogels are then exposed to 395nm UV to crosslink GelMA. After a 4hr stabilization period, three cycles of washing with hexanes is done to remove the surfactant. Nanogels are then stored in hexanes, at room temperature and without light.

A heater was used to maintain the solvent phase at a temperature ~ 40 °C during circulation keeping the GelMA in the liquid phase (**Figure 2.1d**). The GelMA solution is injection through the central channel at a flow rate of 5 µL/min using a syringe pump (**Figure 2.2**). The high flow

rate of the nonsolvent phase allows it to compress the slower flowing solvent phase at the junction of the three channels, forming a thin stream. Diffusion between the two phases along this thin stream leads to the formation of the nanogels. The nanogels are then collected in vials from the outlet in 2 min increments, amounting to ~ 0.5 mL per vial. When the nanogels formed correctly, a fine powder was seen in suspension at this stage, and it took several minutes to settle out of suspension. Nanogel vials were then stored in the dark at room temperature overnight to allow for nanogel stabilization.

A stir bar was placed into each vial and the samples were placed on a stir-plate at 100 rpm for ~ 15 mins to re-disperse the nanogels in toluene. A 395 nm UV lamp (~ 84 mW/cm^2) was set up 16 cm above the stir-plate. The setup was covered in tinfoil, and the lamp was allowed to warm up for ~ 25 mins. Nanogel vials were stirred at 300 rpm and exposed to UV for 25 mins to crosslink, then stored in the dark for 4 h to allow for stabilization before washing. Nanogels were resuspended at 200 rpm for 5 mins then transferred into labelled 1.5 mL microtubes. 500 µL of hexane was added into each microtube and they were placed in the centrifuge for 6 mins at 8.0 G. The samples formed off-white pellets. The supernatant was then carefully removed, and the pellet was washed twice more with 1 mL hexane for 4 mins at 8.0 g, to ensure the removal of the surfactant and toluene. A fine powder was visible after washing along within a solid pellet. Absence of the fine powder and presence of only a hard/gummy pellet, or the presence of visible particles is an indication that the nanogels were not properly formed or crosslinked. The nanogels were then store in 500 µL of hexanes in the dark.

2.6. Optimization of Nanogel Synthesis

To produce loaded nanogels with the potential for use as a smart drug delivery system, the synthesis needed to produce nanogels of a consistent size range and low dispersity. The nanogels should also be stored without aggregation for a period to allow applications in treatments. Variations of key parameters were explored to optimize the synthesis of loaded nanogels and meet the desired outcomes described above.

2.6.1. Determination of Successful Synthesis

Three criteria indicate a successful synthesis of nanogels: The first marker of a successful synthesis was a visual indication of nanogels post sample washing (**Figure 2.3**). In a successful synthesis, the nanogels appeared as a hazy beige ‘powder’ at the bottom of the micro tube (**Figure 2.3a.i**). This ‘powder’ can be resuspended in the solvent with mild agitation and falls out of suspension slowly over several minutes (**Figure 2.3a.ii**). The presence of a hard pellet (**Figure 2.3a**) can indicate clumps of crosslinked GelMA formed by either nanogel aggregation prior to crosslinking, or presence of crosslinked GelMA that failed to form nanogels during microfluidic synthesis due to fluctuations in the flow conditions. The pellets may also indicate the presence of crosslinked nanogels compressed during the centrifuge process, in which case the pellet will soften and break apart into ‘powder’ over time. The presence of a solid pellet that does not soften, and no visible powder (**Figure 2.3b**), indicates an unsuccessful synthesis in which either; nanogels were never formed during microfluidic synthesis, or they were unstable, and aggregated completely before crosslinking. Additionally, if the crosslinking of the GelMA was unsuccessful, the GelMA polymer will form clear fiber-like structures in the solvent (**Figure 2.3c**).

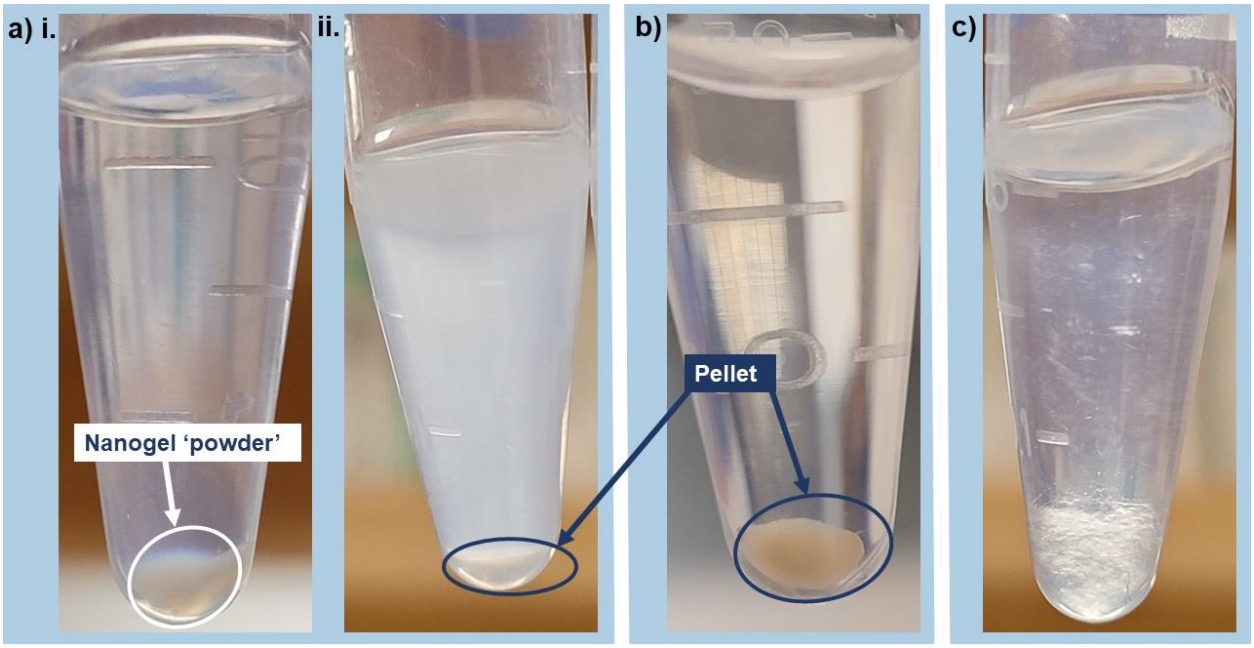

Figure 2.3. GelMA Nanogels Crosslinked vs. Uncrosslinked.
(a) Crosslinked Nanogels. **i.** Nanogels crosslinked 4mins under UV (395nm), washed with hexanes, then stored in hexanes and centrifuged for 4mins at 8G. A beige 'powder' present at the bottom of the microtube indicates successful nanogel synthesis. **ii**. Nanogel 'powder' resuspended. **(b)** Uncrosslinked GelMA forms fiber-like structures in hexanes and falls quickly out of suspension.

The second step used to confirm the successful synthesis of nanogels was the characterization of the samples using a Joel 1011 Transmission Electron Microscope (TEM) to visualize loaded nanogels and dynamic light scattering (DLS) to determine the nanogel size distributions. For TEM imaging, nanogel 'powder' was resuspended using a pipet tip, then depending on the visible concentration of 'powder' present, the nanogels were either loaded directly onto the TEM grid or diluted before loading. Pure C, Carbon 200 mesh, Cu support films were loaded with 5 µL of the sample, allowed to dry in the dark for 48 h and then imaged. TEM images were used to determine the presence of nanogels, give an idea of their size and determine if the Ag NPs were present. For the nanogel synthesis to be considered successful, nanogels within the size range between 80 and 120 nm needed to be present. Additionally, for a successful synthesis of Ag NP loaded nanogels, the Ag NPs had to be present within the nanogels. For DLS, the nanogel

samples were resuspended using the pipet tip, then 100 µL of the sample was diluted in 1 mL of hexane. Diluted nanogels are loaded into a quartz cuvette and each sample was measured in triplicate.

The last indication of successful synthesis is the stability of the suspension in storage conditions. To be functional as a drug delivery system, it is optimal for the nanogels to have a high stability so they can be stored for prolonged periods of time without aggregation. The aggregation of nanogels within 2 weeks of synthesis was considered suboptimal and the synthesis parameters were further adjusted. As crosslinking of the nanogels only renders them insoluble in aqueous solution for a period after which erosion will take place, samples were stored in hexane to increase the time they could be stored. Samples were also kept in the dark, as they are light sensitive. Fully crosslinked GelMA nanogels carry a negative surface charge which affords them colloidal stability due to the repellent forces of like charges [88]. The presence of nanogel clumping within hexane was indicative of inadequate crosslinking to maintain the nanogel's form, as fully crosslinked nanogels should not readily erode in an organic solvent and should have colloidal stability. To remove the nanogels from hexanes and place them in aqueous medium, nanogels were centrifuged and the hexanes removed. Nanogels were then resuspended in DI water and the lid of the microtube was left open to allow any residual hexanes to evaporate. The method of transfer of nanogels from hexanes to aqueous solution would require further optimization prior to cell experiments to ensure no residual hexanes.

2.6.2. Parameter Optimization

The key parameters optimized in this project can be divided into three categories: solvent/non—solvent phase (**Figure 2.4a**), crosslinking conditions (**Figure 2.4b**), and washing/storage conditions (**Figure 2.4c**).

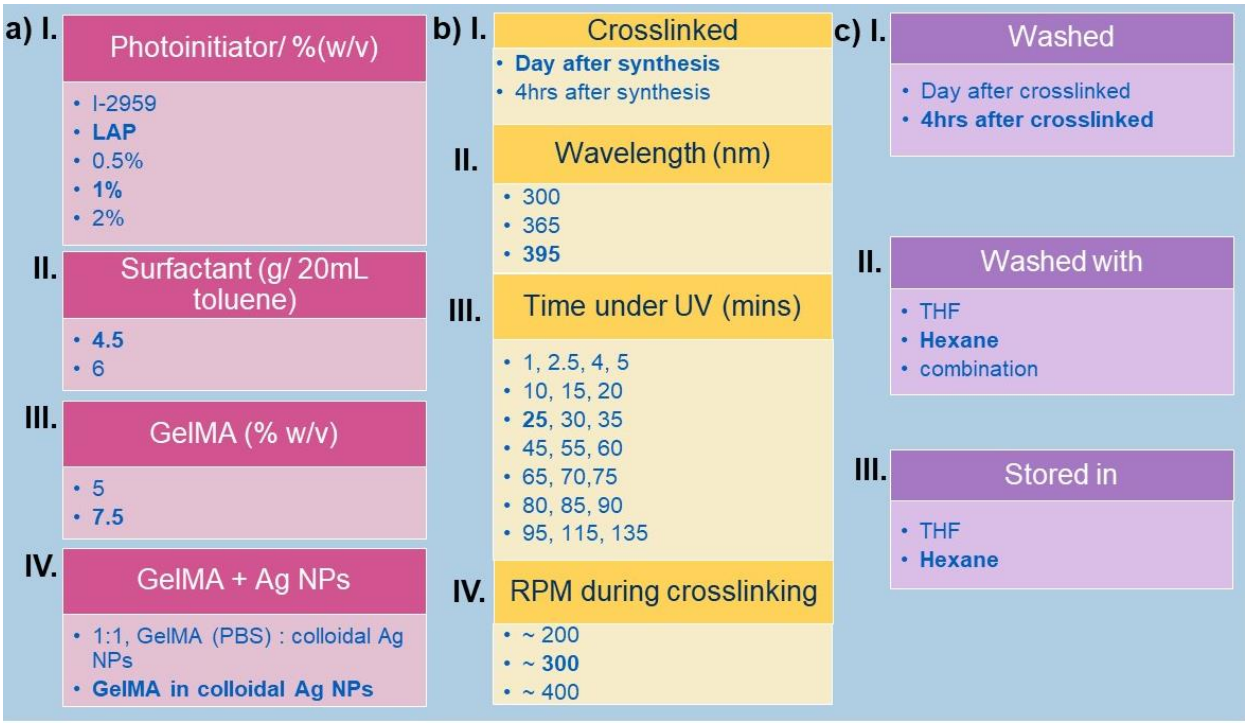

Figure 2.4. Parameters Adjusted for Optimization of Synthesis.

Optimal parameters are indicated in bold. **(a)** Parameters regarding preparation of solvent and non-solvent phases. **I.** Type and amount (in % w/v) of photoinitiator used in solvent phase. **II.** Surfactant (Span-80) is used in the preparation of the non-solvent phase. **III.** Different w/v % of the GelMA polymer were used in the solvent phase. **IV.** Methods for incorporating the Ag NPs into the solvent phase; dissolving the GelMA polymer in PBS then mixing at a 1:1 ratio with colloidal Ag NPs or dissolving the GelMA directly into colloidal Ag NPs. **(b)** Parameters regarding the crosslinking of nanogels. **I.** A shorter (~ 4 h) and a longer (overnight) period of nanogel stabilization prior to crosslinking. **II.** Three different UV wavelengths were used throughout optimization; 300 nm, 365 nm and 39 5nm. **III.** Time allowed for nanogel crosslinking under UV exposure. **IV.** RPM of the stir bar inside each sample vial during the crosslinking process. **(c)** Parameters regarding the washing and storage of nanogels after crosslinking. **I.** Time allowed between cross-linking and washing of nanogels. **II.** Solvent used during nanogel washing process. **III.** Solvent used to store nanogels.

2.6.3. Optimization of Solvent/Non-solvent Phase Parameters

Two different photoinitiators were used at several concentrations (0.5%, 1%, 2% w/v) during synthesis optimization (**Figure 2.4a.I**), 2-Hydroxy-4'-(2-hydroxyethoxy)-2-methylpropiophenone (I-2959) and Lithium phenyl-2,4,6-trimethylbenzoylphosphinate (LAP). I-2959 and LAP are both Type-I radical photoinitiators, or cleavable photoinitiators [66]. The original synthesis used I-2959 at a concentration of 0.5% (w/v) in the solvent phase. However, we lost access to the 300 nm UV lamp originally used the reaction, and the efficiency of I-2959 greatly decreased due to its low molar extinction coefficient at 365 nm and 395 nm (UV wavelengths available) [72]. Higher concentrations of I-2959 were tested (1% and 2% w/v) to circumvent the loss of reaction efficiency. However, difficulties associated with nearing the solubility limit of I-2959 and the association of increased cytotoxicity at higher concentration levels necessitated a change in photoinitiator. LAP was found to consistently produce stable nanogels at a concentration of 1% w/v.

Both 4.5 g and 6.0 g of surfactant (Span80) in the non-solvent phase were tested during optimization (**Figure 2.4a.II**). The surfactant function is to stabilize the nanogels during synthesis and before crosslinking, although it is removed fully during the washing procedure. Increased Span80 (6.0g) in the non-solvent phase did not appear to impact the overall nanogel stability, it did however increase the difficulty of achieving and maintaining a stable jetting of the solvent phase within the junction of the microfluidic chip. A concentration of 4.5 g Span80/ 20 mL toluene was considered optimal for the synthesis.

The original synthesis method [88] used 5.0% (w/v) of GelMA pre-polymer for the solvent phase (**Figure 2.4a.III**). Issues with nanogel stability overtime and aggregation instigated use of

a higher concentration of pre-polymer (7.5% w/v), this improved the number of samples per collection which produced successful nanogels after washing. The higher concentration of 7.5% GelMA pre-polymer was carried forward in the synthesis.

To load Ag NPs into Nanogels, the original synthesis method [88] involved the preparation of the GelMA pre-polymer and photoinitiator solution in PBS (pH7.4) at double the final working concentration (**Figure 2.4a.IV**). The concentrated solution was then mixed with the colloidal Ag NPs at a volume ratio of 1:1 to achieve the desired concentration of pre-polymer solution. This method of addition did not yield loaded nanogels. It was hypothesized that this may be due to the resulting concentration of Ag NPs after dilution by the pre-polymer solution was too low to yield an average of ≥ 1 Ag NPs per Nanogel volume. The solvent phase was then prepared by dissolving the photoinitiator and GelMA pre-polymer directly into the colloidal Ag NPs, without PBS, and this preparation method resulted in Ag NPs present within the nanogels.

2.6.4. Optimization of Crosslinking Parameters

The time interval between nanogel synthesis and crosslinking was explored (**Figure 2.4b.I**). Successful nanogel synthesis was achieved when nanogels were allowed to stabilize for 4 h, or overnight prior to crosslinking was tested. The nanogels were kept at room temperature and without light during the stabilization period. The nanogels that were allowed to stabilize overnight were more consistently successful than those given only 4 h to stabilize.

Three different wavelengths of UV were utilized throughout the optimization process (**Figure 2.4b.II**). The original synthesis performed by Dr. Valente [88] used a 300 nm UV lamp. However, access to this lamp was limited leading to the optimization of the nanogel crosslinking

with the more accessible 365 nm (~ 20 mW/cm^2) and 395 nm (~ 84 mW/cm^2) UV lamps. While crosslinking was achieved with both UV lamps, the higher power of the 395 nm lamp allowed for shorter crosslinking times making the synthesis more efficient.

A large variety of crosslinking times were tested as UV lamps, photoinitiators and GelMA pre-polymer concentrations were adjusted (**Figure 2.4b.iii**). Times tested ranged between 1 – 135 mins, with optimization focusing on the shortest time to obtain successfully crosslinked nanogels. The final crosslinking time of 25 mins produced the most consistent results, although the 4 mins crosslinking time also produced successful nanogels.

The rotation rate (in rpm) of the stir bars during the crosslinking period is an important parameter as it ensures there is enough circulation of nanogels for a uniform UV exposure (**Figure 2.4b.iv**). The original rate used in Dr. Valente's synthesis was 200 rpm. During optimization, the rate was increased to improve the circulation of nanogels under UV illumination, and thereby, help improve the number of nanogels in the sample that are adequately crosslinked. Higher rates (~ 400 rpm) resulted in the nanogels breaking into smaller nanogels before they could be fully crosslinked (**Figure 2.5**). A central value of 300 rpm was optimal, as it allowed adequate circulation of the nanogels, and more even crosslinking throughout the sample without producing the broken nanogels seen at the higher rpm.

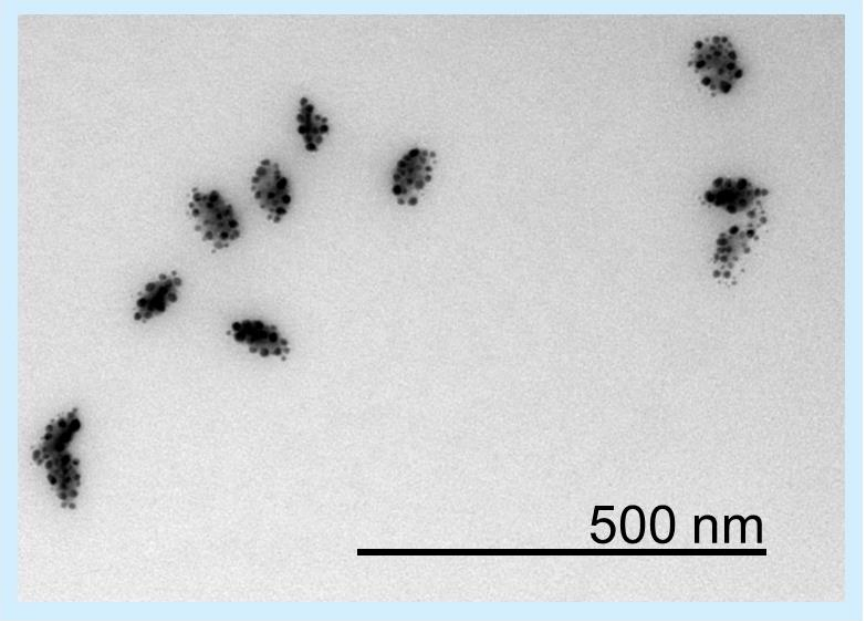

Figure 2.5. Impacts of high rpm during crosslinking.
The nanogels prepared without the addition of Ag NPs, they were crosslinked with ~ 400 rpm.

2.6.5. Optimization of Washing and Storage Conditions.

The impact of the time between crosslinking and washing of nanogels was briefly examined (**Figure 2.4c.I**). Washing the day after crosslinking and ~ 4 h after crosslinking were compared. Samples that were washed the day after crosslinking had no noticeable difference to the ones washed ~ 4 h after crosslinking. Washing ~ 4 h after crosslinking was adopted into the methodology, as it improved the time efficiency of the synthesis.

The original synthesis created by Dr. Valente [88] used tetrahydrofuran (THF) to both wash and store the nanogels post crosslinking (**Figure 2.4c.II, III**). Hexane was first tested for the initial wash of nanogels to explore if it reduced the aggregation of nanogels. More 'powder' was present in samples after the initial hexane wash, but then aggregation would visibly occur when the wash

switched to THF. This led to the use of hexane for all three wash cycles and for the storage of the nanogels.

2.7. *In situ* Synthesis of Silver Nanoparticles in Loaded Nanogels

This synthesis aimed to reduce $AgNO_3$ to Ag NPs inside the nanogels via the UV radiation used for crosslinking. Two different syntheses were attempted, with variations occurring in the composition of the solvent phase. The non-solvent phase remained the same in both syntheses, being prepared with 4.5 g Span80 and 20 mL toluene.

2.7.1. Solvent Phase for *In Situ* synthesis of silver nanoparticles using 25 mM $AgNO_3$

A solution of 50 mM $AgNO_3$ was prepared with deionized water. GelMA pre-polymer (degree of methacrylation, 0.0158 mmol/g) and I-2959 were dissolved into 0.5 mL of PBS (pH7.4), leading to concentrations of 15% and 2% (w/v) respectively. The solvent phase was then prepared by mixing the $AgNO_3$ solution and the GelMA pre-polymer solution in a 1:1 ratio for final concentrations of 7.5% (w/v) GelMA pre-polymer, 1% (w/v) I-2959, and 25 mM $AgNO_3$. The solvent phase produced was cloudy white and was then warmed in the oven < 50 °C to obtain a usable viscosity.

2.7.2. Solvent phase for *in situ* synthesis of silver nanoparticles using 6.25 mM $AgNO_3$

The $AgNO_3$ solution was prepared at a concentration of 12.5mM. The GelMA pre-polymer solution was prepared by dissolving GelMA pre-polymer (degree of methacrylation 0.0199 mmol/g) at 15% (w/v) and LAP at 4% (w/v) in PBS (pH7.4). The $AgNO_3$ solution was mixed at a

1:1 ration with the GelMA pre-polymer to obtain a solvent phase with final concentrations of 7.5% (GelMA), 2% (LAP), and 6.25mM $AgNO_3$. The solvent phase was then warmed to optimal viscosity in the oven < 50C°.

2.7.3. Fabrication of loaded nanogels with *in situ* synthesis of silver nanoparticles

The microfluidic synthesis of encapsulated silver nanoparticles nanogels using both the 25 mM $AgNO_3$ and 6.25 mM $AgNO_3$ followed the same procedure as the other nanogel synthesis described above. After formation, the nanogels were allowed to stabilize in the dark at room temperature overnight. The nanogels were then resuspended using a stir bar at 100 rpm. A 365 nm UV was then used to crosslink the nanogels for 115 mins, with the stirring rate set at 300 rpm. After crosslinking, a colour change from a cloudy white to a cloudy tan is observed (**Figure 2.6.** Colour change of *in situ* loaded nanogels after UV exposure.), indicating a reducing of the $AgNO_3$.

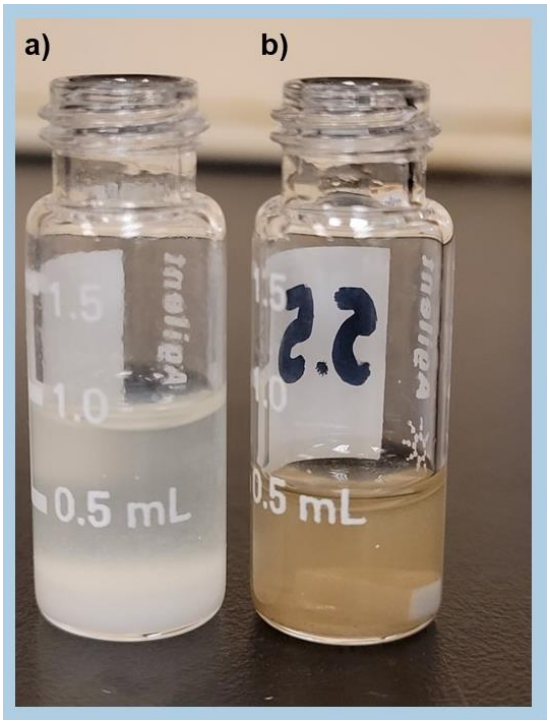

Figure 2.6. Colour change of *in situ* loaded nanogels after UV exposure.

(a) *In situ* Nanogels without UV exposure. **(b)** *In situ* nanogels after UV exposure.

Nanogels were then allowed to sit for ~ 4 h before washing. Stir bars were used to resuspend the nanogels for 10 mins @ 180 rpm, then the suspension was transferred to microtubes. Hexane was added to the microtubes, and the tubes were vigorously agitated by hand, then centrifuged at 8.0 G for 6 mins. Pellets were formed by the nanogels, the supernatant was removed, and fresh hexane was added. This procedure was repeated twice more, for a total of three washes, with the centrifuge time dropping to 4 mins after the initial wash. The nanogels were then stored in hexanes and placed in the dark at room temperature.

In situ loaded nanogels were then imaged using TEM to assess the success of the Ag NP synthesis and nanogel loading (**Figure 2.6b**). To prepare nanogels for TEM imaging, TEM grids (Carbon 200 mesh, Cu) were loaded with 5 µL of sample, which has been agitated using the pipette to cause resuspension of the nanogels. If the nanogel sample was visibly highly concentrated, it was diluted with additional hexane before loading (generally either a 5x or 10x dilution). TEM grids were then allowed to dry for 48 h at room temperature without light.

DLS was also used to assess the size distribution of the nanogels. Nanogel samples, after resuspension, were diluted at 10 µL to 990 µL of hexane, then loaded into a quartz cuvette for measurements. All measurements were taken in triplicate.

Chapter 3 Characterization and Particle Release:

3.1. Results of Fabrication of Loaded Nanogels with *In Situ* Synthesis of Ag NPs

The synthesis of Ag NP loaded nanogels proved challenging and required extensive optimization of the methodology, as indicated in **Figure 2.4**. Loading the nanogels with Ag NPs was particularly difficult because a high concentration of Ag NPs suspension was required to achieve ≥ 1 Ag NP per nanogel volume. One potential solution was to reduce $AgNO_3$ to produce Ag NPs directly inside the nanogels using UV irradiation. Ultimately, the challenge of producing nanogels loaded with Ag NPs was overcome through the preparation of the solvent phase directly in colloidal Ag NPs. However, the methodology and result of the *in situ* synthesis has been included since it presents the possibility of a simple synthesis for Ag NP loaded nanogels.

The *in situ* reduction of $AgNO_3$ inside nanogels via UV irradiation is relatively simple and eliminates the requirement of additional chemical reducing agents [89]. *In situ* reductions of $AgNO_3$ into NPs or nanoclusters by UV radiation has been previously performed in the literature for hydrogels [58], microgels [90] and nanogels [89]. Reithofer et al. reduced $AgNO_3$ to Ag NPs in a peptide hydrogel [58]. Their methodology involved direct mixing of $AgNO_3$ into the hydrogel solution pre-crosslinking, followed by gelation of the hydrogel in the dark. Subsequently, UV radiation at 254 nm was used to facilitate the reduction of $AgNO_3$. Zhang and coworkers developed an *in situ* synthesis of Ag nanoclusters inside microgels in 2005 [90]. They first created poly(N-isopropylacrylamide-acrylicacid-2-hydroxyethyl acrylate) microgels via precipitation polymerization and crosslinked the microgels with 4 mol-% N,N′-methylene bisacrylamide. Once formed, the microgels were soaked in aqueous $AgNO_3$ solution before being exposed to 365 nm

UV for varying time intervals. Zhao and colleagues performed an *in situ* synthesis of Ag NPs inside of genetically engineered polypeptide nanogels [89]. The nanogels were synthesized by boiling of the polypeptide in water followed by cooling and renaturation. The nanogels were then soaked in a solution of $AgNO_3$ and I-2959 before exposure to UV irradiation, allowing simultaneous crosslinking and reduction the $AgNO_3$ into Ag NPs. In their synthesis, Zhao et al. utilized I-2959 at 1% (w/v), relying on the ketyl radicals produced by its decomposition to reduce the Ag^+ to Ag^0. To the best of our knowledge, the literature did not contain an example of *in situ* Ag NP synthesis in nanogels that employed direct mixing of $AgNO_3$ into the pre-polymer nanogel solution prior to the nanogel synthesis.

Our fabrication of loaded nanogel with *in situ* synthesis of Ag NPs was informed by the methodologies described by Zhao et al. and by Reithofer and colleagues. It employed the direct mixing of $AgNO_3$ into the pre-polymer solution to avoid an additional step of soaking the nanogels, as described by Reithofer et al. [58]. Incorporation of a photoinitiator for the simultaneous photo-crosslinking of the nanogel and aid in the reduction of the $AgNO_3$ was an approach adapted from the synthesis of Zhao and collaborators [89].

3.1.1. Fabrication of loaded nanogels with *in situ* synthesis of Ag NPs using 25mM $AgNO_3$

The *in situ* loaded nanogels synthesis performed using 25 mM $AgNO_3$ and I-2959 as the photoinitiator was only moderately successful. Samples had only a small amount of visual "powder" after the washing procedure, indicating poor formation of nanogels. TEM grids, loaded immediately after washing, confirmed the presence of nanogels (**Figure 3.1**). However, all samples were completely aggregated 4 days post washing, indicating a lack of stability. TEM

images indicated the average size of Ag NPs formed was 47 ± 40 nm, indicating high polydispersity (**Figure 3.1**). The average size was calculated from 70 Ag NP diameters obtained from the TEM images using ImageJ software. Reithofer and colleagues reported an Ag NP size range of 10-20 nm for the *in situ* synthesis of Ag NPs in a peptide hydrogel, working with both 10 mM and 20 mM concentrations [58]. Despite working at a similar concentration of $AgNO_3$, the results obtained in our synthesis reflected far less uniformity of Ag NPs and a much larger average size. It should be noted that, while our concentration and addition method of $AgNO_3$ followed Reithofer et al., their synthesis did not employ photoinitiators and used hydrogel instead of nanogels, which may impact the Ag NPs formation. Zhao et al. worked with nanogels and a photoinitiator to produce Ag NPs of 15.7 nm to 20.6 nm using concentrations of 0.25 mM and 2.5 mM respectively, although they did not provide any standard deviation values for these size measurements [89]. Their paper suggested that the Ag NP size can be controlled by the $AgNO_3$ concentration [89]. A relationship between concentration of $AgNO_3$ and size of Ag NPs could explain the large size of Ag NPs produced by our synthesis. However, both Zhao et al. and Reithofer et al. reported only a small size dispersity in their Ag NPs, which may indicate that the Ag NPs observed in **Figure 3.1** are a result of aggregation. The larger size and broader size range obtained by our synthesis is not ideal for the intended purpose of the nanogel system, as the radiosensitizing effect of Ag NPs decreases with increased particle size [91]. Additionally, the large size will hinder the Ag NP's ability to diffuse out of the pores of the nanogel after swelling and could reduce the efficiency of the size dependent tumor permeation [30].

Nanogels produced by our 25 mM $AgNO_3$ synthesis contain either a single Ag NP or aggregate of Ag NPs which take up a significant portion of the nanogel's volume (**Figure 3.1.**

TEM of *in situ* loaded nanogels 25mM AgNO3.), making the possibility of release of the Ag NP without full erosion of the nanogel unlikely. It can also be seen in (**Figure 3.1**) that several of the smaller Ag NPs formed are not encompassed by a nanogel.

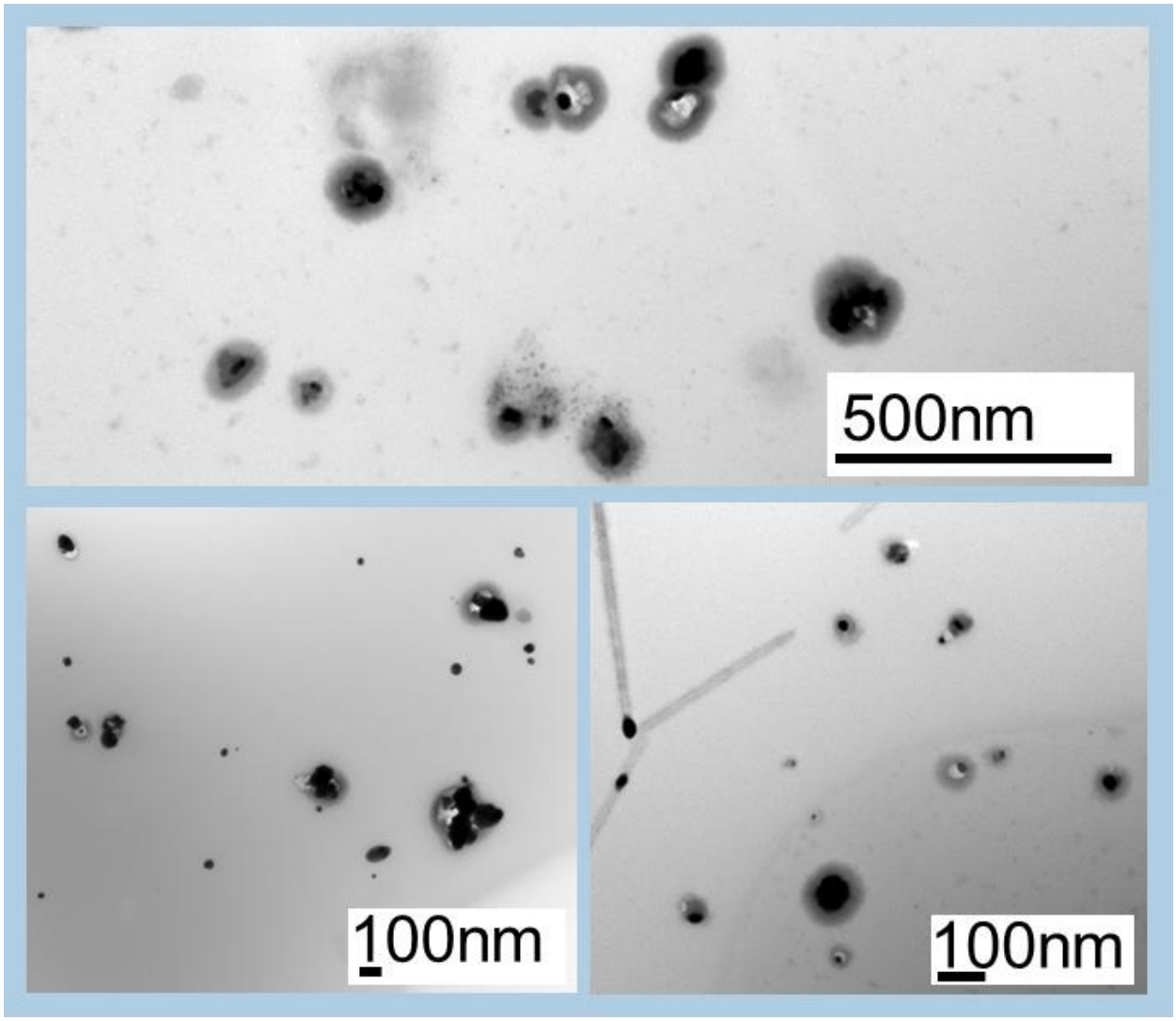

Figure 3.1. TEM of *in situ* loaded nanogels 25mM $AgNO_3$.

TEM images of *in situ* synthesized nanogels captured at 80 K magnification. TEM grids (Support Films, Carbon 200 mesh, Cu) were loaded with 5 μL of sample, dried for ~ 48 h in the dark then stored without light until imaged. The presence of both Ag NPs (black) and GelMA (grey), Ag NPs and Nanogels are heterogenous in shape and size. Solvent phase was prepared with a 1:1 mixture of 50 mM $AgNO_3$ (aq) and GelMA solution (15% GelMA, 2% I-2959), for final concentrations of 7.5% GelMA, 1% I-2959 and 25 nM $AgNO_3$. Nanogels were collected at solvent and non-solvent flow rates of 5.5 μL/min and 400 μL/min respectively and crosslinked for 115 mins with a 365 nm UV.

This could be explained by incomplete crosslinking. as the I-2959 has a low molar extinction coefficient at 365 nm [76] which may result in not all nanogels receiving enough UV irradiation to fully crosslink. Nanogels with lower exposure to UV would contain fewer chemical crosslinks between polymer chains [62]. The degree of methacrylation of the pre-polymer used in this synthesis was an order of magnitude lower than the pre-polymer used to successfully synthesize loaded nanogels (0.0158 vs 0.1584 mmol/g), contributing to lower levels of chemical crosslinks. Reduced numbers of chemical crosslinks can cause larger pore sizes and increased susceptibility to erosion when compared to fully crosslinked nanogels [92]. Unencapsulated Ag NPs could also be an indication that the nanogels were not consistently formed during the microfluidic synthesis. The partial crosslinking of the nanogel may also contribute to the size dispersity seen in **Figure 3.1**. The hydrogel functions as the stabilizer for the Ag NPs and erosion or large pores in the polymer network would reduce its functionality as a stabilizer, allowing for more aggregation.

3.1.2. Fabrication of loaded nanogels with *in situ* synthesis of Ag NPs 6.25 mM $AgNO_3$

The optimization of loaded nanogels with pre-synthesized Ag NPs occurred in parallel to the attempts at *in situ* syntheses. That optimization led to the change of photoinitiator from I-2959 to LAP, due to LAP's increased absorption at 365 nm. The *in situ* synthesis was adjusted to incorporate LAP at 2% (w/v) to improve the crosslinking of the nanogels. A change to the concentration of $AgNO_3$ was also made to decrease the size of Ag NPs formed. The *in situ* synthesis of Ag NPs using 6.25mM and 2% LAP as the photoinitiator was more successful than the higher concentration synthesis. Two days post crosslinking the nanogels samples had moderate amounts of fine powder present and notable resuspension (**Figure 3.2**), compared to the minimal powder seen in the higher concentration synthesis after washing. This is indicative of an increased

concentration of successfully synthesized nanogels. Nanogels of the lower concentration synthesis only began to aggregate 5 days post synthesis, compared to the higher concentration synthesis which saw complete aggregation at 4 days post synthesis.

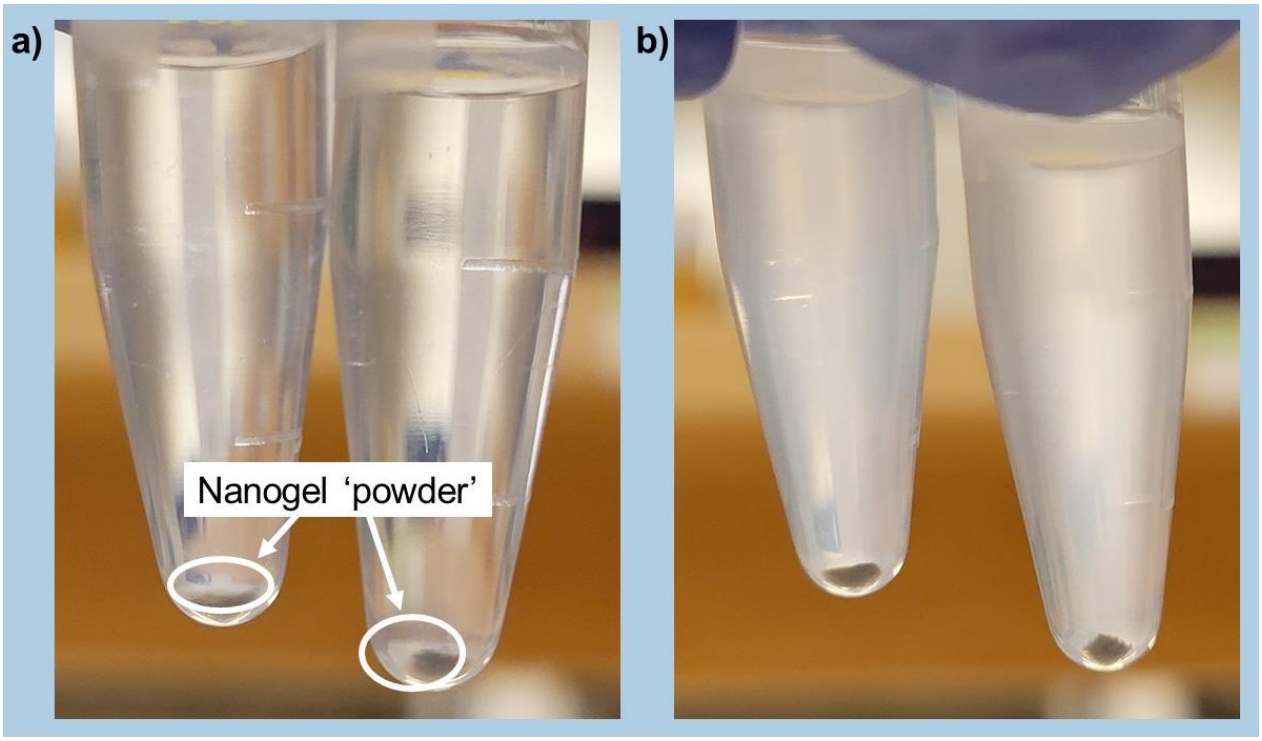

Figure 3.2. Nanogel resuspension from *in situ* 6.25mM $AgNO_3$ synthesis.
In situ Ag NP nanogels synthesized with 6.25mM $AgNO_3$ and 2% (w/v) LAP, two days post crosslinking. **a)** Nanogel samples after centrifugation, with nanogel "powder" indicated. **b)** Nanogel samples resuspended in hexanes.

TEM grids, loaded immediately after washing were imaged revealing that the $AgNO_3$ was successfully reduced to form Ag NPs (**Figure 3.4**). ImageJ software was used to measure the TEM images of 719 Ag NPs (**Figure 3.3**) formed using the lower concentration of $AgNO_3$. The average size was then calculated to be 8 ± 3 nm. This is significantly smaller and less polydisperse than those formed using 25 mM $AgNO_3$, which agrees with the relationship between $AgNO_3$ concentration and Ag NP size reported by Zhao and colleagues [89].

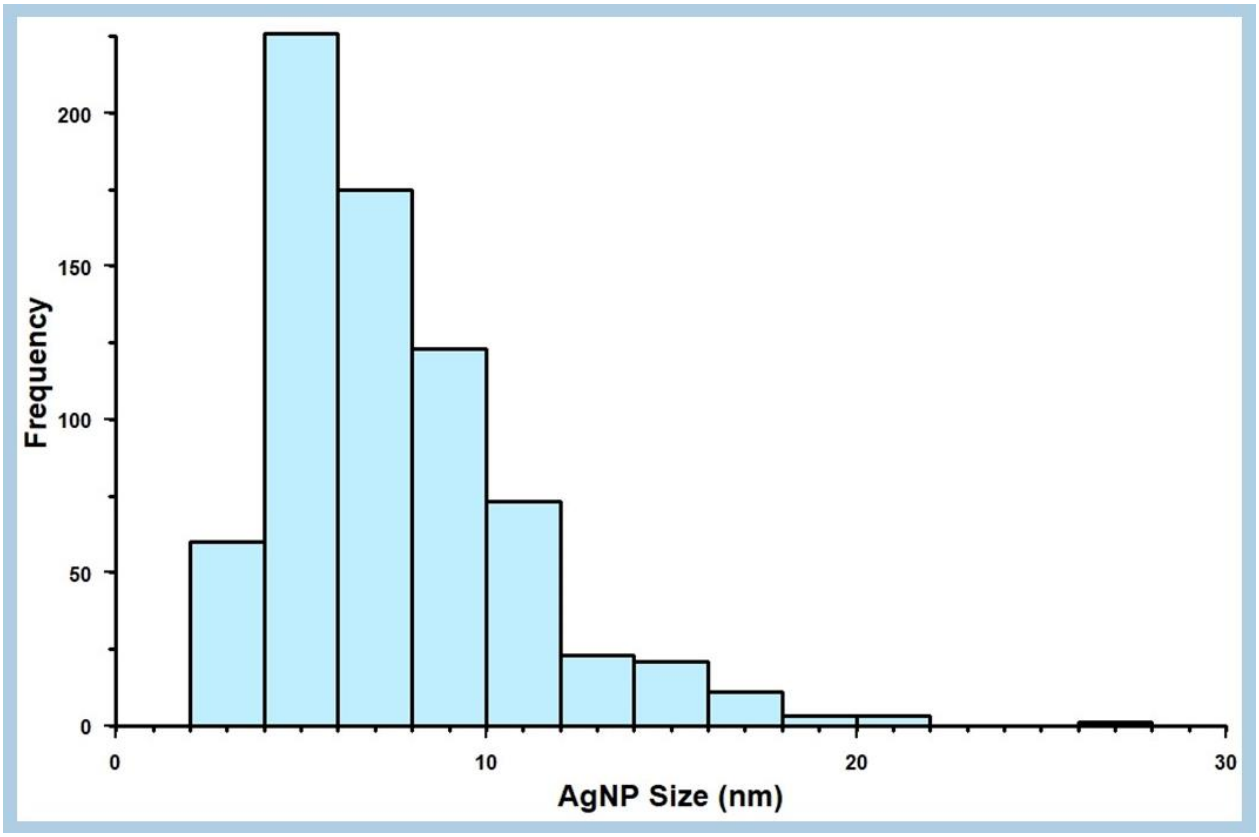

Figure 3.3. Size distribution of Ag NPs from *in situ* synthesis.
Size distribution of Ag NPs formed by the *in situ* synthesis using 6.25 mM $AgNO_3$. Measurements were taken from 12 TEM images of 719 Ag NPs using ImageJ software. Ag NPs were measured where nanogels were in adequate focus to allow for reasonable measurement of the Ag NPs.

The Ag NPs from the low concentration synthesis still presented in a range of sizes, with the presence of some aggregates between 40-60 nm (**Figure 3.4c**). The 6.25 mM $AgNO_3$ synthesis also yielded an average of 22 ± 11 Ag NPs present in each nanogel, compared to the single Ag NP present in the 25 mM $AgNO_3$ synthesis. TEM images were used to count the number of Ag NPs per nanogel for 33 nanogels to provide the average. The reduction in Ag NP aggregation seen in this synthesis compared to the 25 mM synthesis could be the result of the switching of the photoinitiator from 1-2959 to LAP. LAP has a significantly higher absorption at 365nm than I-2959 [72], which would result in a higher degree of chemical crosslinking in the nanogels [62], improving stability and reducing pore sizes.

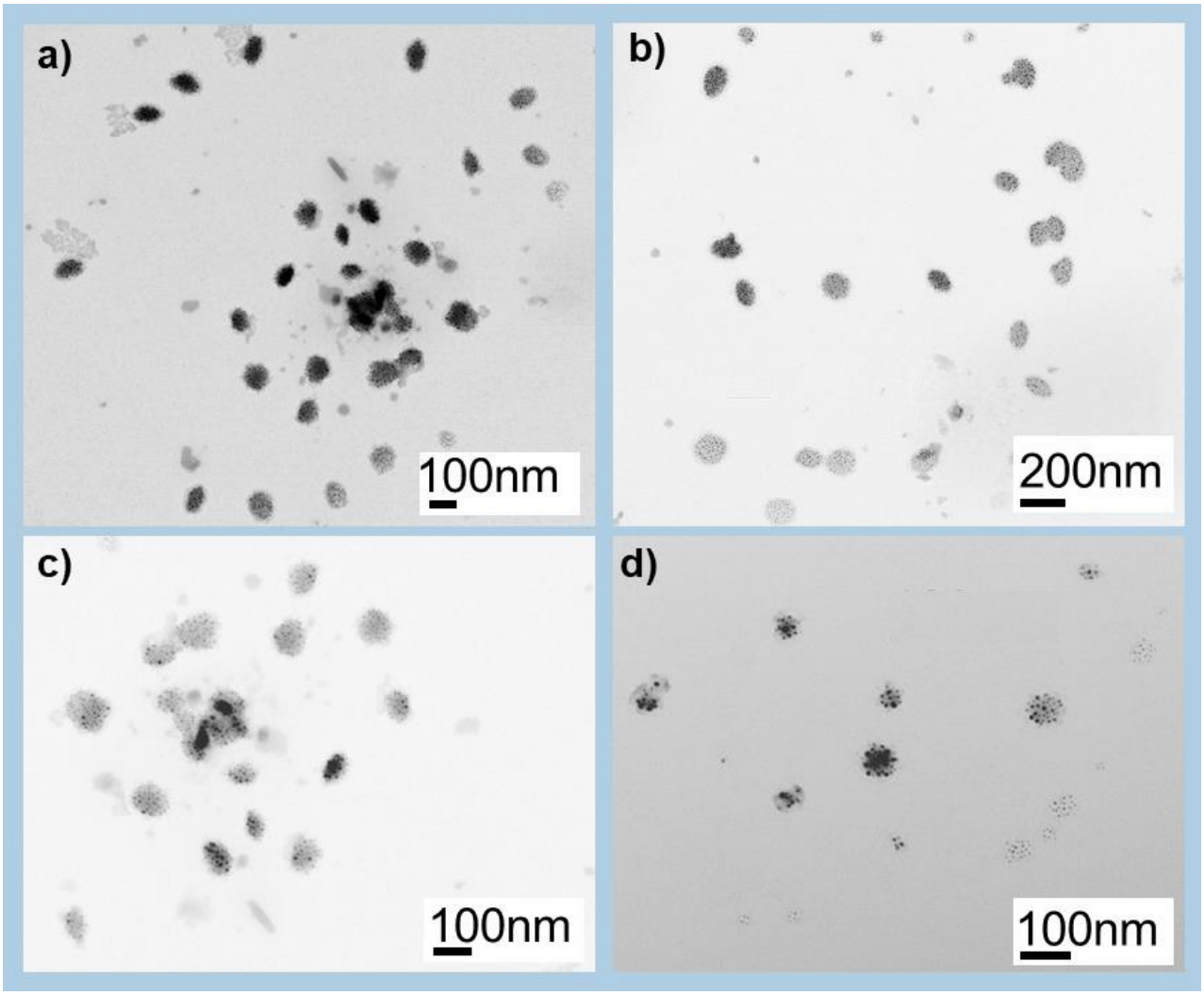

Figure 3.4. TEM of *in situ* loaded nanogels 6.25 mM $AgNO_3$.
Solvent phase composed of 1:1 GelMA solution (15% GelMA, 4% LAP) and 6.25 mM $AgNO_3$ (aq), for final concentrations of 7.5% GelMA, 2% LAP, and 6.25 mM $AgNO_3$ (aq). TEM image (80 k magnification) of *in situ* loaded nanogels in hexanes, TEM grids (support films, carbon 200 mesh, Cu) loaded with 5 μL sample and dried without light for 48 h before imaging.

This is supported by the increased presence of "powder" seen in the sample collected (**Figure 3.2**), and by the increased length of time before the sample aggregated compared to the rapid aggregation of the 25 mM sample. Additionally, the degree of methacrylation of the pre-polymer used in this synthesis was higher (0.0199 vs 0.0158 mmol/g) than the pre-polymer used in the 25 mM synthesis, contributing to higher levels of chemical crosslinks. The improved stability and

smaller pores of the nanogel would allow it to function better as a stabilizer and prevent the aggregation of the Ag NPs.

The size and dispersity of the nanogels were characterized using DLS (**Figure 3.5**). DLS measures the scattering intensity of incident light over time caused by particles in solution. The fluctuations in scattering intensity are caused by the particle's movement in solution, which is dictated by the particle size as larger particles diffuse slower than smaller particles. An autocorrelation is used to correlate the scattering intensity fluctuations and time, to determine how rapidly the intensity fluctuates. The speed of intensity fluctuations is then related to the movement of the particle in solution, and the diameter of a spherical particle which would exhibit the same motion within the solvent is reported [93].

The samples were composed of two peaks indicating two particle populations. The first population of nanogels represents ~89.9% of the sample intensity and indicates an average nanogel diameter of 233 ± 52 nm with a polydispersity index (PDI) of 0.25. This is larger than the nanogels observed in the TEM images (**Figure 3.4**) which were determined to be 84 ± 30 nm. This was calculated by finding the average of 150 nanogel measurements from TEM images using ImageJ software. The discrepancy, in part, results from the TEM being of dried nanogels while the DLS measurement is taken with nanogels in hexane. However, the difference in sizes observed by DLS and TEM may also result from sample aggregation. The TEM grids were loaded immediately following the washing of the sample, and some aggregation can already be seen (**Figure 3.4**). The DLS however was performed a few days after the synthesis completion, and while samples were not entirely aggregated, the aggregation of two or three smaller nanogels would explain the larger diameters recorded by the DLS. The presence of aggregation is also supported by the appearance

of the second peak on the DLS (**Figure 3.5a**), indicating a population of nanogels at an average of 3405 ± 546 nm. Furthermore, the PDI (24.9%) of the *in situ* loaded nanogels is high when compared literature accounts of loaded nanogels synthesized via microfluidics and loaded nanogels produced by nano emulsion [34,85].

a)

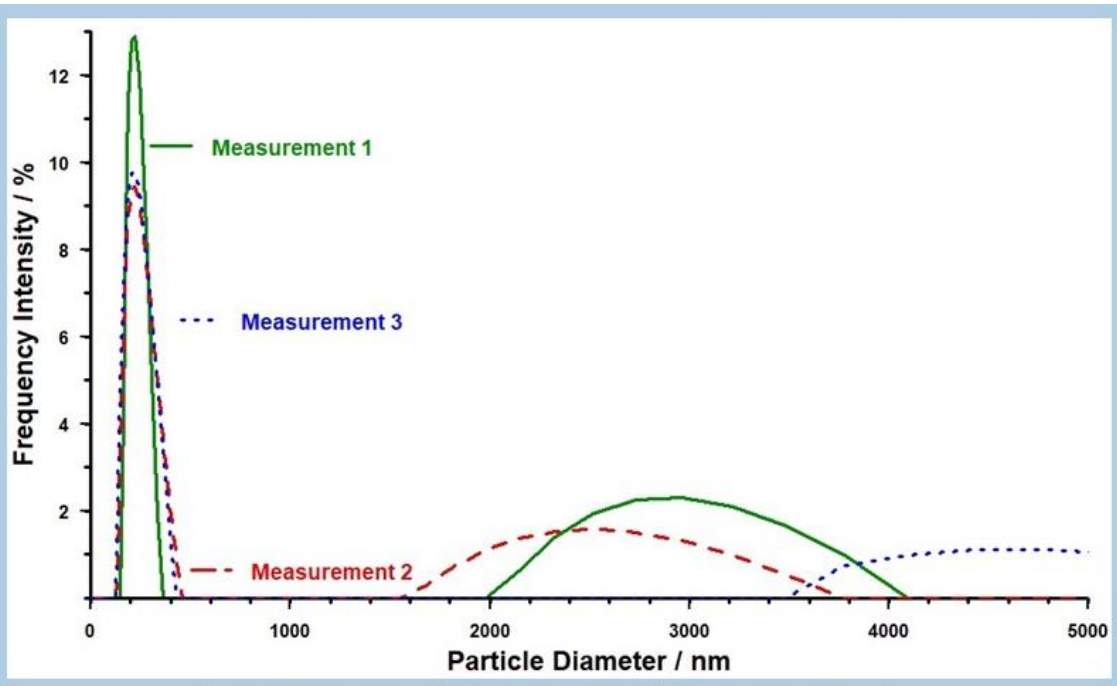

b)

	Peak 1 Particle diameter (nm)	Area 1 (intensity) %	Peak 2 Particle diameter (nm)	Area 2 (intensity) %
Measurement 1	227 ± 41	86.8	2920 ± 461	13.2
Measurement 2	240 ± 59	89.1	2518 ± 477	10.9
Measurement 3	233 ± 55	93.9	4779 ± 699	6.1
Average	**233 ± 52**	**89.9**	**3405 ± 546**	**10.1**

Figure 3.5. DLS of *in situ* loaded Nanogels.

Nanogels synthesized with solvent phase composed of 6.25 mM $AgNO_3$ (aq), 7.5% GelMA pre-polymer, and 2% (w/v) LAP. **a)** Three DLS measurements of particle size dispersity in hexane representing 100% of the sample, taken consecutively. Measurements were taken using a quartz cuvette containing 10 μL sample : 990 μL solvent. **b)** Table indicating the particle diameter and the area (intensity) % of each peak reported. Particle diameter ± the standard deviation reported for the peak by DLS software. The Average diameter is reported ± the standard deviation of the 3 diameters reported. The area (intensity) % reported indicated the percentage of the total signal's intensity that is represented by that peak.

Mahmoudi and colleagues used a hydrodynamic flow focusing microfluidic chip to produce alginate nanogels carrying transforming growth factor beta 3 [85]. The nanogels produced in their study were 125 ± 7 nm with a reported PDI ≤ 0.2. Kang et. al. used a nano emulsion to prepare GelMA nanogels loaded with doxorubicin and reported a PDI of 0.16 [34].

The *in situ* synthesis of Ag NPs using 6.25 mM $AgNO_3$ and LAP as the photoinitiator had greater success when compared to the 25 mM $AgNO_3$ synthesis using I-2959. However, the nanogels produced were still not optimal for the desired purpose. The ideal size to allow for accumulation in a cancerous tumor due to the EPR effect would be between 100-200 nm [34]. The nanogels produced here had a reported range of 182-285 nm by DLS and 54-114 nm by TEM. DLS measurements were taken in an organic solvent (hexane), so the size of the nanogels would be expected to be even larger in an aqueous solvent due to the hydrogel's hydrophilic nature. Additionally, the size of Ag NPs is extremely important as it impacts their diffusion from the nanogel, ability to permeate the tumor, biological interactions, performance as radiosensitizers and how they accumulate/cleared from the body [18,94]. Further optimization was required to allow for lower ploydispersity Ag NPs as well as smaller nanogels with better stability to produce the desired smart drug delivery system. The optimized parameters obtained later for the loaded nanogels using pre-synthesized Ag NPs (**Figure 2.4)** may provide a good starting point to increase the stability of in situ nanogels.

3.2. Results of Loaded Nanogel Synthesis

The original microfluidic synthesis of nanogels loaded with Ag NPs performed by Dr. Valente [88] was extensively optimized. Key changes were made here, including switch of GelMA pre-polymer concentration from 5% to 7.5% (w/v); change of photoinitiator from I-2959 to LAP at 1% (w/v); preparation of solvent phase in colloidal Ag NPs instead of PBS; and the use of a 395 nm UV lamp instead of a 300 nm. The changes to the methodology allowed for the successful synthesis of GelMA nanogels loaded with Ag NPs.

3.2.1. Characterization of Ag NPs

Colloidal Ag NPs with a bare (citrate) surface were purchased from NanoCompsix for the synthesis of loaded nanogels. The purchased Ag NPs were characterized via TEM, DLS, Zeta and UV-Vis. TEM images of the Ag NPs are shown in **Figure 3.6a**. 233 particles were measured using ImageJ and the average particle diameter was calculated to be 11 ± 3 nm, which falls within the 10.0 ± 2.1 nm reported by NanoCompsix. Three DLS measurements were taken at a dilution of 1 µL Ag NPs to 990 µL DI water (**Figure 3.6b**). The average hydrodynamic diameter of the three measurements was calculated to be 16 nm, compared to the 15 nm reported by the manufacturers. The Zeta potential of Ag NPs was taken in triplicate, with a mean Zeta potential (mV) provided for each measurement. Average Zeta potential of -29 mV was then calculated for the sample, aligning well with the -28 mV reported by NanoCompsix. Additionally, the UV-Vis spectra of the purchased Ag NPs were obtained. The recorded λ_{max} of 404 nm, differs from the 391 nm reported by the manufacturer. However, literature indicates an expected λ_{max} of around 400 nm for

10nm Ag NPs stabilized by citrate [95]. The λ_{max} also has been documented to have a red shift as the particle size increases, with a study done by Agnihotri et. al. reporting λ_{max} values of 398, 401 and 406 nm for 10, 15 and 20 nm Ag NPs respectively [96]. DLS and TEM measurements done on the purchased Ag NPs indicate a particle population slightly larger than reported by the manufacturer which could account for the higher λ_{max} value.

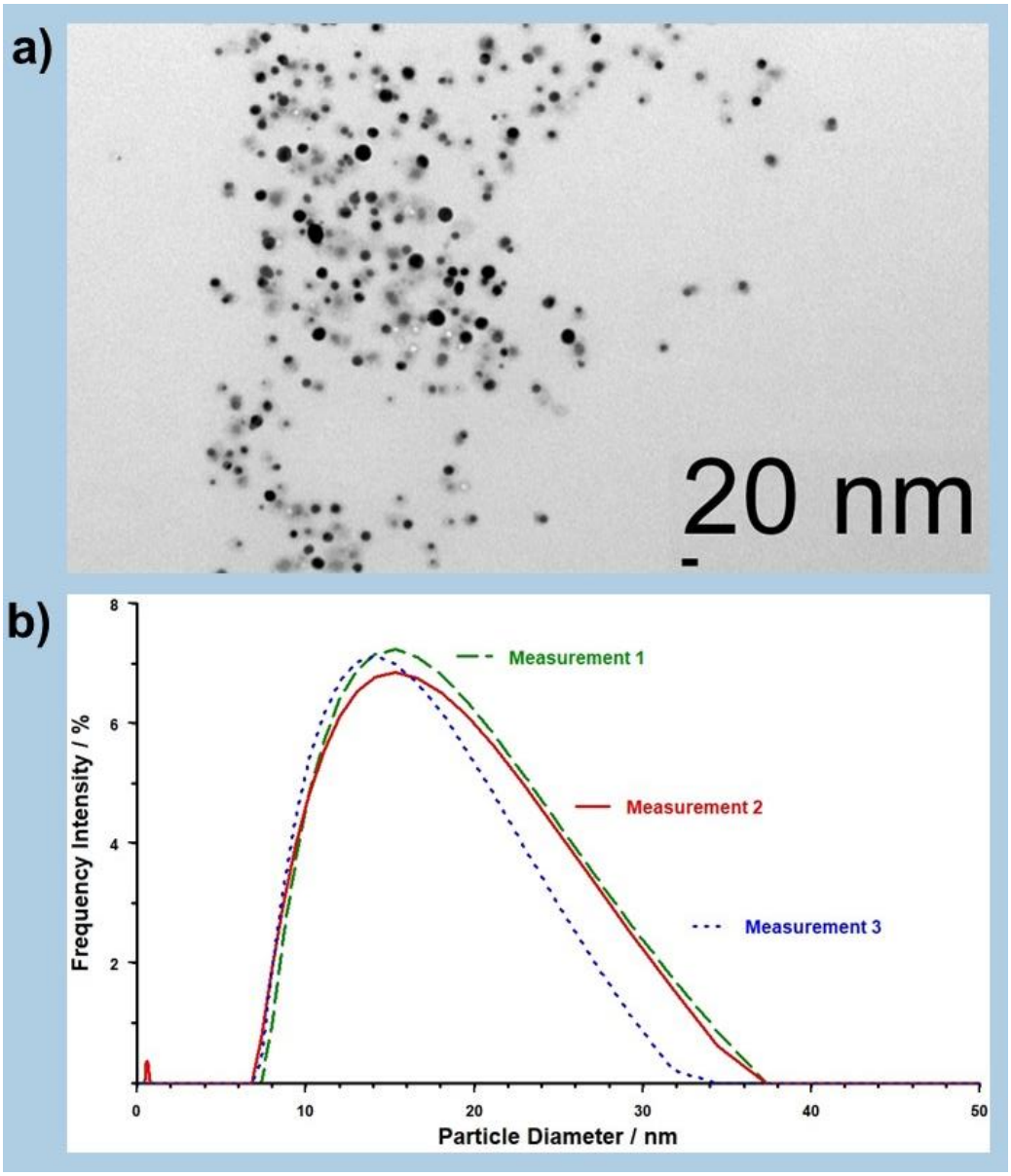

Figure 3.6. TEM and DLS of Ag NPs.

TEM image of 10 nm bare (citrate) Ag NPs purchased from NanoCompsix. **a)** DLS measurement of size distribution taken at a 10x dilution in a disposable cuvette. **b)** Formvar 200 mesh, Cu TEM grid was loaded with 5 μL of the colloidal Ag NPs and dried in the dark for 24 h before imaging. Images taken at 80 K magnification on a Jeol JEM-1011 TEM.

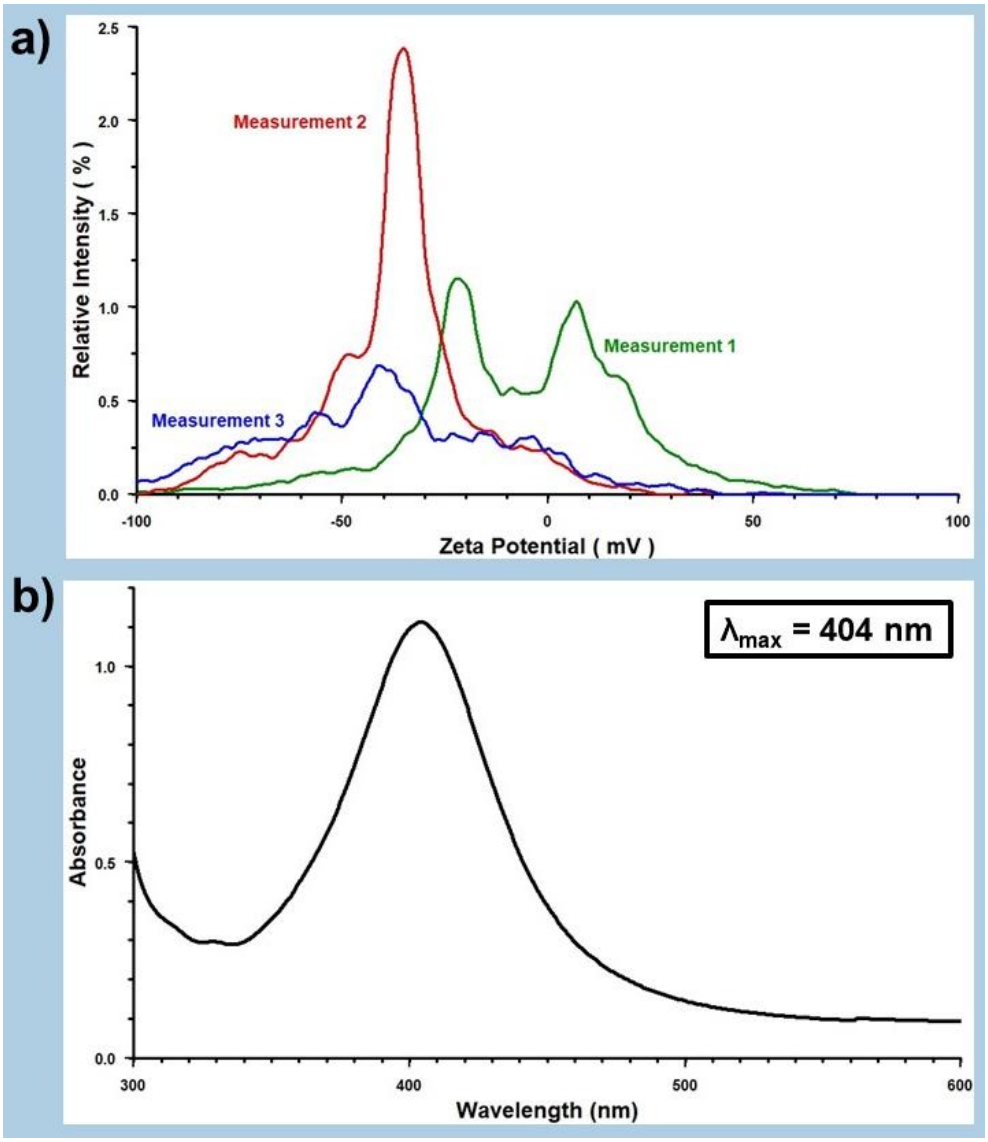

Figure 3.7. Zeta potential and UV-Vis spectra of Ag NPs.
a) Zeta potential recorded at the same 10x dilution measured in an Omega Cuvette. **b)** UV-Vis spectra taken on a Lambda 1050 UV/VIS/NIR Spectrometer.

3.2.2. Characterization of Loaded Nanogels

Optimization discussed previously in Chapter 2.6 allowed for the successful synthesis of Ag NP loaded nanogels using a flow focusing microfluidic device. The loaded nanogels produced were characterized by TEM and DLS. TEM images obtained showed the presence of Ag NPs as small black dots, due to their higher electron density, inside the larger and lighter nanogels (**Figure**

3.8). ImageJ software was used to measure TEM images of 105 nanogels for a calculated average size of 80 ± 25 nm. Analysis of the Ag NPs inside nanogels using ImageJ showed an average size of 5 ± 1 nm.

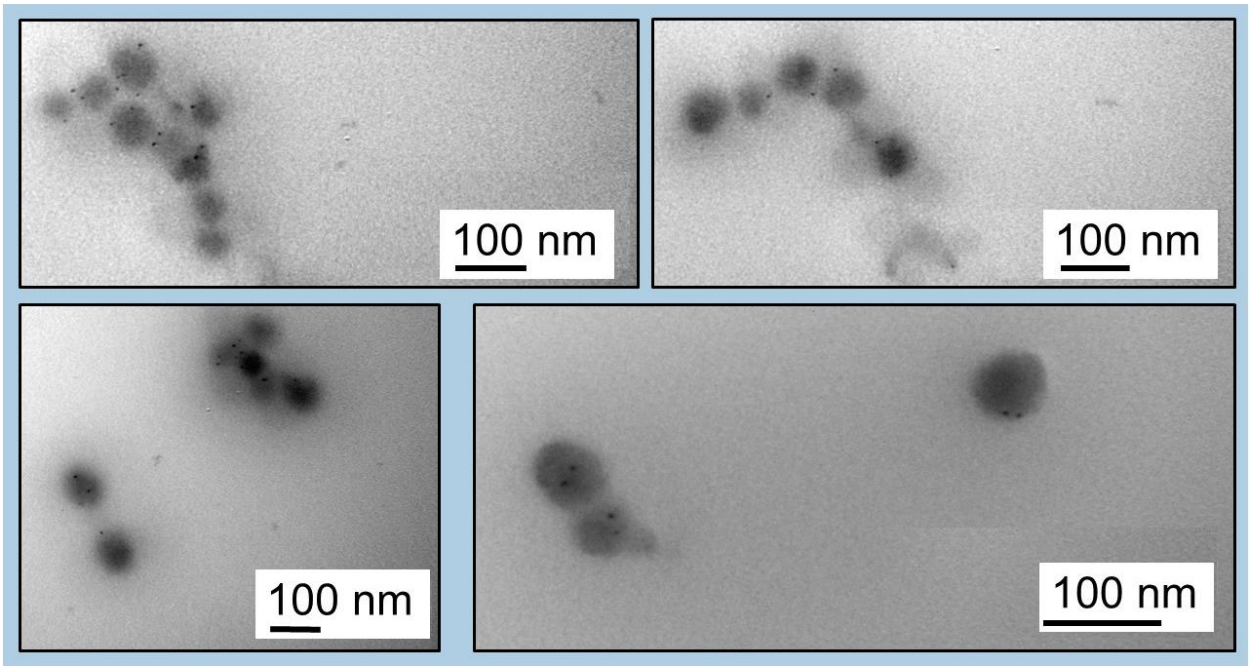

Figure 3.8. TEM images of Ag NP loaded Nanogels.
Solvent phase prepared with GelMA (7.5% w/v), and LAP (1% w/v) dissolved in colloidal Ag NP (NanoCompSix). Nanogels were collected at flow rates of 5 μL/min : 400 μL/min for the solvent and non-solvent phases respectively. Nanogels were stored in hexanes, 5μL of the nanogel sample was loaded on each TEM grid (Pure C, carbon 200 mesh, Cu support films) and allowed to dry in the dark for ~ 48 h before imaging. Images taken at 80 K magnification.

Differing from the larger values found by TEM (11 ± 3 nm) and DLS (16 nm) characterization for the colloidal Ag NPs. The decrease of size observed in the Ag NPs is likely the result of exposure to UV irradiation during nanogel crosslinking. UV irradiation has been demonstrated to cause a decrease in size of citrate stabilized Ag NPs in solution [97]. Analysis of TEM images showed low levels of Ag NP loading in our nanogels with an average of 2 ± 1 Ag NPs per nanogel.

The size of nanogels found through analysis of TEM images is smaller than the desired 100-200 nm range for partial accumulation with the tumor [34]. However, TEM images show dried

nanogels, and its size would be increased in a wet environment due to the porous nature of the nanogel. DLS measurements, taken of nanogels suspended in hexane, provide an indication of nanogel size in a solvent (**Figure 3.9a**). Three DLS measurements were taken of the nanogel sample in hexane, and an average hydrodynamic diameter of 123 ± 2 nm was calculated (**Figure 3.9b**). This falls within the 100-200 nm range reported to be ideal for passive accumulation within cancerous tumors [34]. However, as hexane is an organic solvent there is little to no swelling present in the nanogels, the hydrodynamic diameter of the nanogels in an aqueous medium would be expected to be larger as the nanogels would undergo some degree of swelling (pH dependent). As such DLS measurements in a solvent more representative of bodily conditions would likely place the nanogels outside the desired size range for EPR effect. Our reported size of loaded nanogels is larger than that reported in the original synthesis by Dr. Valente, which was 65 ± 12 nm. This can be partially attributed to the changes made to the solvent phase, as our increase in pre-polymer concentration (5-7.5% (w/v)) would impact the viscosity of the solvent phase. The viscosity of the solvent/non-solvent phases influences the flow rate ratio in the microfluidic synthesis. In flow focusing microfluidic systems, the nanogels are formed by precipitation, and the mixing time between solvent and non-solvent phases is key parameter for dictating nanogel size [84]. The length of the channel and flow rate of both phases dictate the mixing time. Channel length is a fixed parameter, so nanogel size can be increased by increasing the ratio between the solvent phase flow rate and the non-solvent phase flow rate [84]. The solvent phase flow rate used in our synthesis was higher than the one used by Dr. Valente (4.5 µL/min vs 5.0 µL/min), resulting in a higher ratio of flow rates and increased nanogel size. The PDI for DLS measurements were 0.08, 0.03, 0.07 with a sample average of 0.06 (**Figure 3.9b**), indicating low polydispersity.

a)

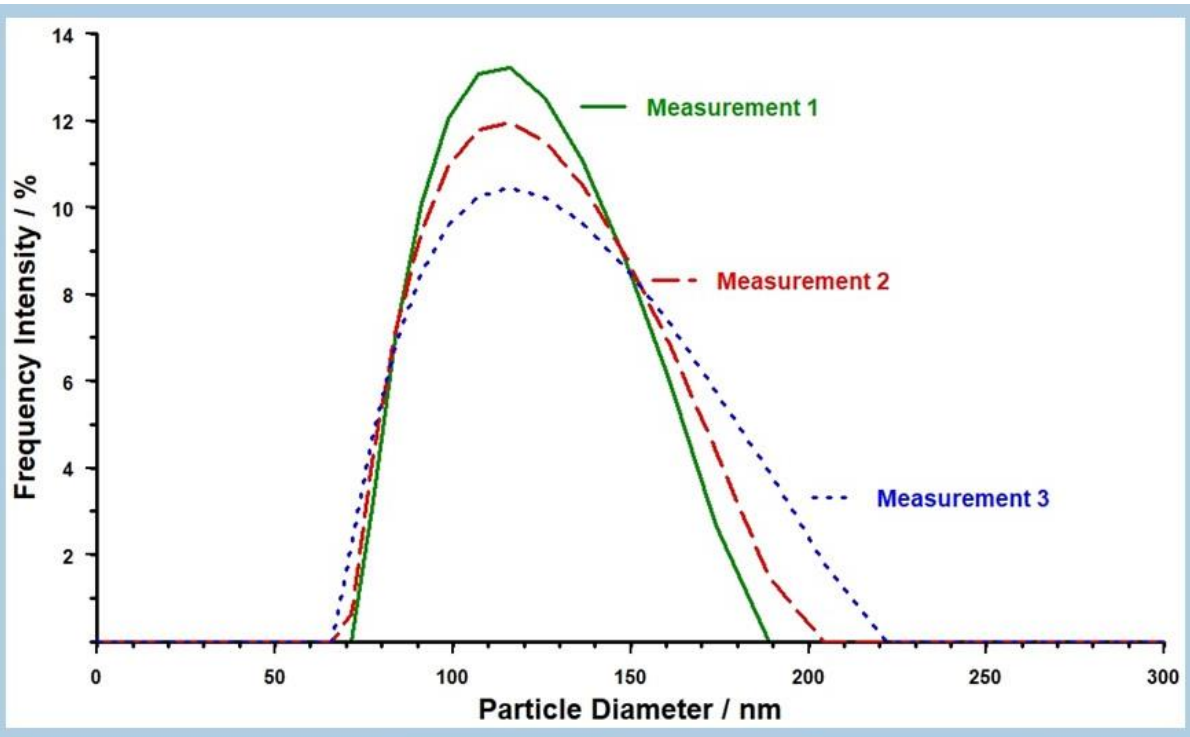

b)

	Measurement 1	Measurement 2	Measurement 3	Average
Polydispersity Index (%)	0.08	0.03	0.07	**0.06**
Hydrodynamic Diameter (nm)	125	122	122	**123 ± 2**

Figure 3.9. DLS of loaded Nanogels in hexane.

(a) Samples were diluted (1 mL hexane : 100 μL sample) then ~ 1 mL of sample was loaded into a quartz cuvette and DLS measurements were taken consecutively (black, red, blue). **(b)** Polydispersity index and hydrodynamic diameter were recorded for each measurement. For each measurement 100% of the sample intensity was captured under the single peak.

These polydispersity values are favorably comparable to those reported in the literature for other nanogels synthesized via microfluidics. The previously discussed microfluidic synthesis of alginate nanogels by Mahmoudi et. al. reported a PDI of 0.13 for 43 ± 4 nm nanogels and a higher PDI of 0.2 for 125 ± 7 nm nanogels. Huang and colleagues preformed a microfluidic synthesis of hyaluronic acid nanogels of varying sizes, loaded with therapeutic proteins for the intracellular delivery [98]. The loaded nanogels produced had sizes between 78.4 – 91.5 nm and reported PDIs between 0.10 and 0.16.

a)

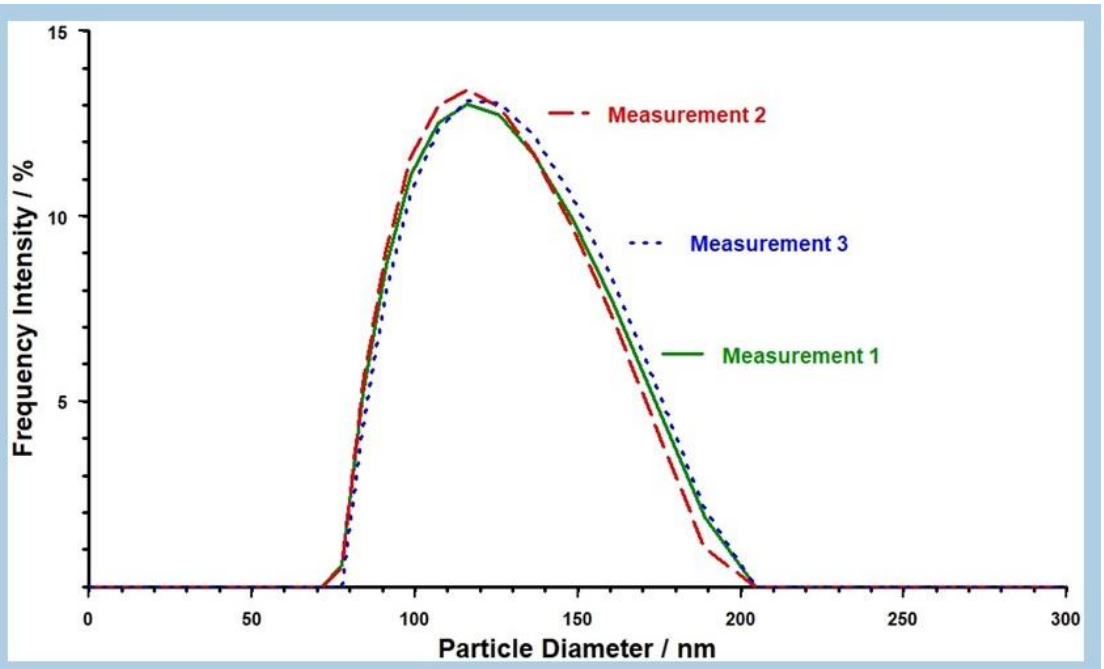

b)

	Measurement 1	Measurement 2	Measurement 3	Average
Hydrodynamic Diameter (nm)	141	131	130	**134 ± 6**
Polydispersity index	0.05	0.12	0.10	**0.9**

Figure 3.10. DLS of loaded nanogels 44 days post synthesis, in hexane.

Nanogels were stored in the dark at room temperature in hexanes. **(a)** Samples were diluted (1 mL hexane : 100 μL sample) then ~ 1 mL of sample was loaded into a quartz cuvette and DLS measurements were taken consecutively (black, red, blue). **(b)** Polydispersity index and hydrodynamic diameter recorded for each measurement. For each measurement 100% of the sample intensity was captured under the single peak.

DLS measurements of nanogels produced by our synthesis were also taken 44 days post synthesis, to explore the stability of the nanogel (**Figure 3.10a**). The nanogels were stored without light in hexane over the 44-day period, then three DLS measurements were obtained. The average hydrodynamic diameter was calculated to be 134 ± 6 nm. The PDI of the nanogels after 44 days were 0.05, 0.12, 0.1 for a sample average of 0.09 (**Figure 3.10b**). Hydrodynamic diameter is still within the desired size range for biological application, and the PDI remains low indicating a still

relatively low-polydisperse nanogel population. This supports the nanogels being stable for a time frame that could reasonably allow for biomedical applications.

Overall, the synthesis of Ag NP loaded nanogels was a success, producing low-polydisperse nanogels that remain stable for over 6 weeks. Nanogels had low levels of loading (< 2 Ag NPs/nanogel), although high Z number nanoparticles, such as Ag, have been shown to provide significant radiosensitizing effects even at very low concentrations. Bromma and colleagues showed that 15 nm gold NPs could provide radiosentizing effects at concentrations as low as 0.2 nM of gold nanoparticles [99]. The theoretical concentration of Ag NPs produced by our synthesis was found to be ~ 70 nM. The theoretical concentration was calculated by first using the flow rates and collection time to determine the number of nanogels per sample (2.6×10^{13} per 0.8mL). Then the average loading of < 2 Ag NPs per nanogel was applied to determine a concentration of Ag NPs. These calculations operate on the assumption that 100% of the solvent phase is converted into nanogels. Given 70 nM is significantly larger than the 0.2 nM, the Ag NP concentration obtained by this synthesis should be sufficient to produce radiosensitizing effect despite low loading. However, if we assume an average cell volume of ~ 2000 μm then the concentration of 0.2 nM Ag NPs would translate to ~240 Ag NPs per cell volume. With that in mind the loading efficiency of this synthesis requires further optimization, as at the currently level of < 2 Ag NPs per nanogel you would need clinical concentrations that amounted to more than 120 nanogels per cancer cell.

3.3. Release of Ag NPs from Nanogel

The release of the Ag NPs from the nanogel in acidic conditions was explored using DLS. The samples were centrifuged at 8G for 6 minutes and the supernatant (hexane) was removed. The sample was then resuspended in 1 mL of either DI water, or DI water lowered to pH 5-6 using 0.001 M nitric acid. To dilute the samples for DLS measurements 200 µL of the sample was added to 1 mL of the corresponding DI water or DI water pH 5-6. Three DLS measurements were then taken consecutively. DLS reports an average hydrodynamic diameter for a measurement, and the most prevalent hydrodynamic diameter for each peak. The reported hydrodynamic diameter for measurements resulting in one peak is that of the measurement average. For measurements that resulted in more than one peak, the most prevalent hydrodynamic diameter is reported for each peak. Notably, pH of the laboratory DI water had been determined to be slightly basic (~ 7-8 pH) 2 months prior to release experiment using pH strips. The DI water was tested again using pH strips after the DLS results of the release were obtained, revealing the DI water had shifted to an acidic pH around 6-7.

The DLS obtained from nanogels in DI water shows an increase in average nanogel size over consecutive measurements and the appearance of a second peak in the final measurement (**Figure 3.11a**). Measurement 1, 2 show single peaks reporting a hydrodynamic diameter in hexane of 516 ± 84 nm and 625 ± 117 nm respectively. Measurement 3 shows a main peak with hydrodynamic diameter in hexane of 892 ± 363 nm and a smaller peak with a hydrodynamic diameter of 82 ± 15 nm.

DLS obtained from nanogels in DI water lowered to pH 5-6 also shows increasing average size of nanogels over consecutive measurements and the appearance of a second peak in all but the first measurement (**Figure 3.12**). Measurement 1 reports a single peak with a hydrodynamic

diameter if 424 ± 42 nm. Measurements 2 and 3 both show a large peak, 685 ± 154 nm and 1048 ± 265 nm respectively, and a smaller peak, 61 ± 8 nm and 151 ± 17 nm respectively. Nanogels have larger hydrodynamic diameters in aqueous solutions than in hexanes, due to the hydrophilic nature of the hydrogel. The pH sensitive nature of the nanogel this increase in hydrodynamic diameter compared to those seen in hexane will be exaggerated further in an acidic environment due to the increased swelling.

a)

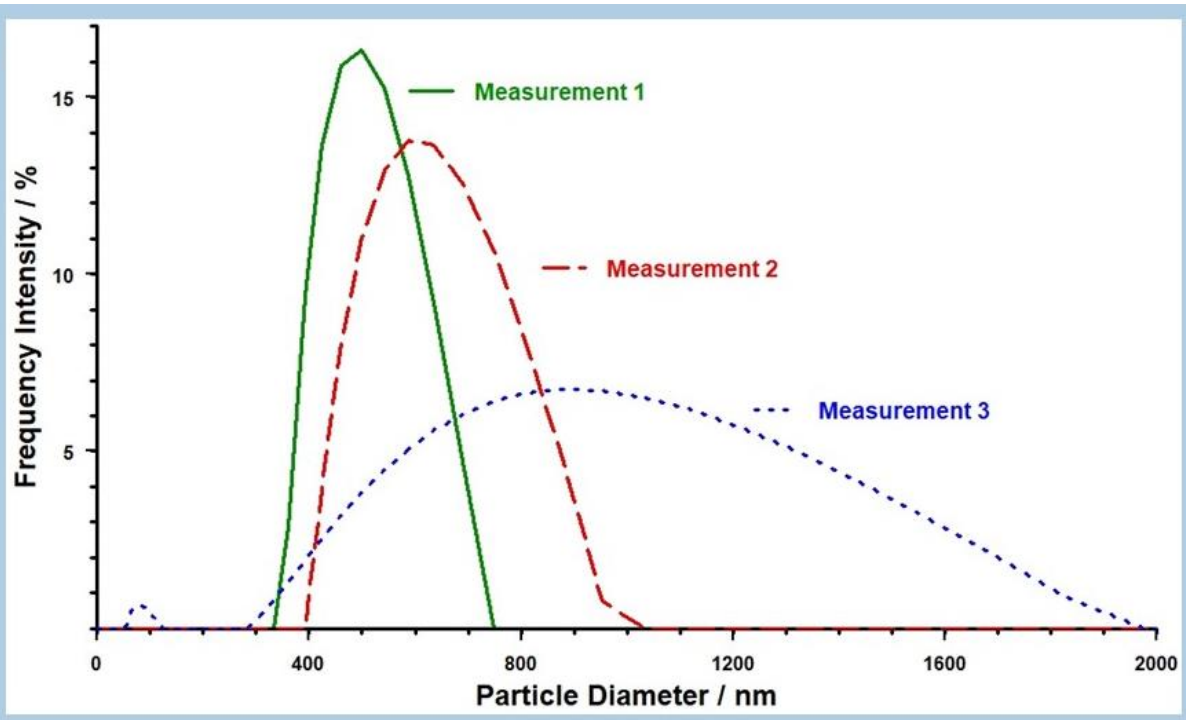

b)

	Hydrodynamic Diameter Peak 1 (nm)	Hydrodynamic Diameter Peak 2 (nm)
Measurement 1	516 ± 84	-
Measurement 2	625 ± 117	-
Measurement 3	892 ± 363	82 ± 15

Figure 3.11. DLS of Loaded Nanogels in DI Water, pH 6-7.
a) Three consecutive measurements of loaded nanogels in DI water. **b)** Hydrodynamic diameter assigned to each peak.

As expected, DLS reports much larger hydrodynamic diameters for loaded nanogels in DI water at pH 6-7 and pH 5-6 than the 123 ± 2 nm reported for the loaded nanogels in hexanes (**Figure 3.9b**). DLS results for both DI water pH 5-6 and 6-7 also indicate the increase in hydrodynamic diameter over the time the DLS was acquired (**Figure 3.12** and **Figure 3.11**). Loaded nanogels in pH 6-7 increased from 516 ± 84 nm to 625 ± 117 nm to 892 ± 363 nm. Loaded nanogels in pH 5-6 saw a larger increase, with consecutive hydrodynamic diameters of 424 ± 42 nm, 685 ± 154 nm and 1048 ± 265 nm. The GelMA pre-polymer used for this synthesis was demonstrated to swell at pH 6, in comparison to pH 7.4 [88]. GelMA is prone to quicker erosion in aqueous environments [92]. Due to the pH sensitive nature of the GelMA pre-ploymer used in our synthesis, the nanogels have increased susceptibility to erosion with increasing acidity. Erosion of nanogels and subsequent aggregation would explain both the large hydrodynamic diameters observed and the increasing range of those diameters.

Notably, the DLS obtained in the pH 6-7 medium, a second peak occurs in measurement 3 at a much smaller hydrodynamic diameter of 82 ± 15 nm (**Figure 3.11**). A smaller second peak also occurs in measurements 2 and 3 of pH 5-6 nanogels, at 61 ± 8 nm and 151 ± 7 nm respectively (**Figure 3.12**). The presence of these peaks could be accounted for by one of two explanations. These peaks could potentially indicate the release of Ag NPs from the nanogels. The hydrodynamic diameter indicated by these peaks is smaller than what would be expected for the nanogels in an acidic aqueous solution. A subset of smaller nanogels would also be expected to be seen on all three DLS measurements and not just in the final one or two. The Ag NPs used in the synthesis were characterized by DLS to be 16 nm, while TEM analysis of loaded Ag NPs suggested a diameter of 5 ± 1 nm. The smaller peaks captured in pH 6-7 and 5-6 DLS indicate hydrodynamic

diameters much larger than single Ag NP. This could be explained by the released Ag NPs having residual nanogel attached to them from the erosion and release process. Hydrodynamic diameter relates the hydrodynamic friction exhibited by the particle being examined, to the diameter of a perfect sphere that would exhibit the same hydrodynamic friction. Ag NPs with residual nanogel attached would experience higher hydrodynamic friction, and an increased hydrodynamic diameter estimated by the DLS. The aggregation of Ag NPs once released, due to the acidic environment is also a plausible explanation for the size of the secondary peaks in **Figure 3.11** and **Figure 3.12**. Bélteky et. al. reported the aggregation of citrate stabilized 10 nm Ag NPs in an acidic pH between 5-7 with an increase in the size of aggregations over time [100].

a)

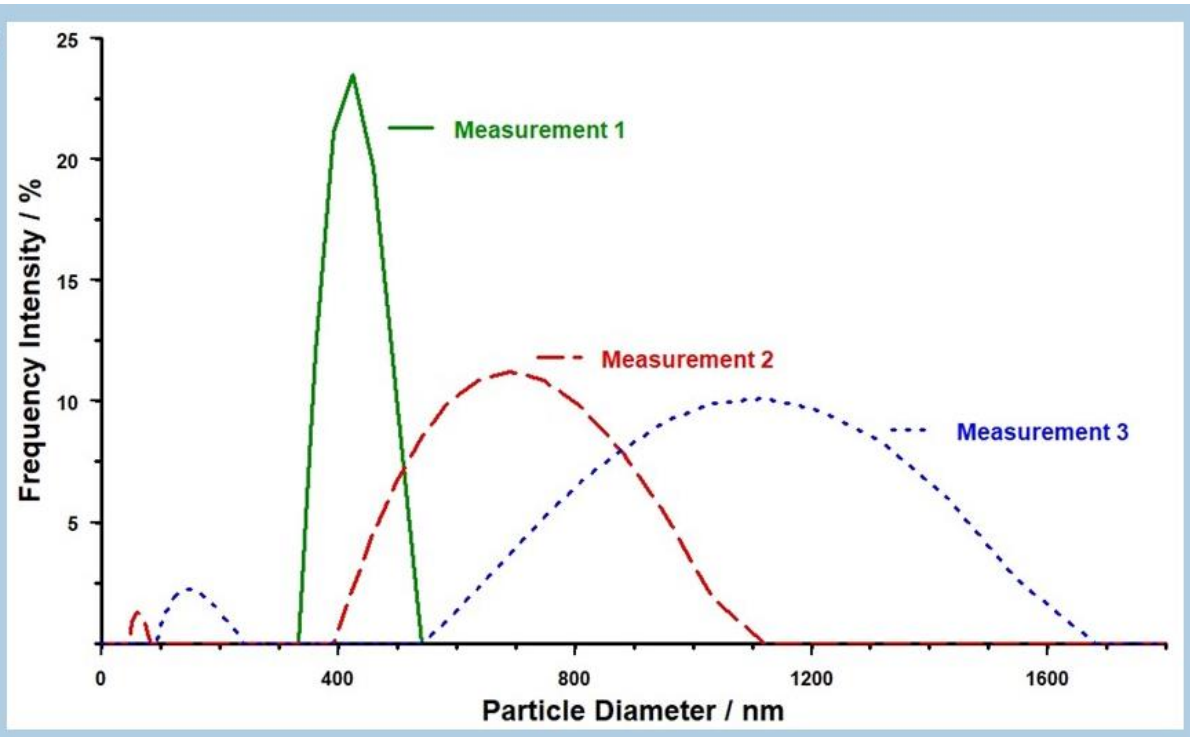

b)

	Hydrodynamic Diameter Peak 1 (nm)	Hydrodynamic Diameter Peak 2 (nm)
Measurement 1	424 ± 42	-
Measurement 2	685 ± 154	61 ± 8
Measurement 3	1048 ± 265	151 ± 17

Figure 3.12. DLS of Loaded Nanogels in DI Water pH 5-6.
(a) Loaded nanogels were placed in DI water with pH 5-6. Three measurements were taken consecutively. **(b)** Reported most prevalent hydrodynamic diameter, the largest peak is considered "Peak 1".

An alternative, and more plausible explanation for the presences of the secondary peaks is that they are a fitting artifact produced by the autocorrelation software. Continuous distributions can be highly variable especially as distribution peaks broaden, leading to the production of secondary peaks by the autocorrelation function in order to fit the particle distribution. This is supported by the intensity reported for the secondary peaks. DLS results are reported directly from a Malvern machine, which reports intensity Ag NPs are known to have strong scattering and absorption interactions with light, as the conduction electrons on their surface undergo collective

oscillation when excited by light in a process known as surface plasmon resonance (SPR). Nanogels do not undergo SPR, and so have weaker scattering interactions with incident light. It would then be expected that the scattering intensity reported for released Ag NPs would be relatively high in comparison to that of nanogels. The intensities of the secondary peaks in **Figure 3.11** and **Figure 3.12** are significantly lower than what would be expected for Ag NPs.

The results described above may indicate that the Ag NPs are released from the nanogels in an acidic environment. The appearance of the smaller secondary peaks in the later measurements of both **Figure 3.11** and **Figure 3.12** could be attributed to the expected release of the Ag NPs. The discrepancy between the size of characterized Ag NPs and the hydrodynamic diameter reported in the release experiments can be explained through either the presence of residual nanogel attached to the Ag NPs or by the aggregation of Ag NPs in an acidic environment. However, these peaks can also be plausibly explained as a fitting artifact of the autocorrelation function. An explanation supported by the low intensities of the secondary peaks. Determination of the reproducibility of the secondary peaks would be needed to reduce the plausibility of a fitting artifact being their cause.

Chapter 4 Conclusions

This work outlined the optimization and synthesis of pH-sensitive Ag NP loaded nanogels using a microfluidic device and presented preliminary results on the release of the Ag NPs. The use of microfluidics in the synthesis of nanogels presents the opportunity for increased control over size/dispersity, and a reduction in volumes of reagents required for synthesis. The *in situ* synthesis of Ag NPs inside the pH-sensitive nanogels showed potential for a simplistic synthesis without the requirement of additional Ag NP synthesis, purchase, or soaking. UV irradiation at 365 nm wavelength was shown to successfully reduce $AgNO_3$ into Ag NPs with a size range of 8 ± 3 nm determined through TEM image analysis. TEM images also indicated relatively high levels of Ag NP loading in each nanogel, reporting an average of 22 ± 11 Ag NPs/nanogel. The nanogels produced by the *in situ* synthesis were less successful than the Ag NPs. TEM analysis reported a nanogel size of 84 ± 30 nm, while DLS of the nanogels in hexanes reported a large hydrodynamic diameter of 233 ± 52 nm. The PDI of the *in situ* loaded nanogels was 0.25, indicating a more polydisperse population than achieved by other microfluidic based synthesis [85,98]. *In situ* loaded nanogels lacked the stability required for them to be used for biological applications, evident by a peak at 3465 ± 546 nm in the DLS and by visual aggregation of the samples after 5 days. Low stability is attributed, in part, to low levels of methacrylation in the GelMA pre-polymer. The *in situ* synthesis reported in this work shows promising formation and loading of Ag NPs. The high loading efficiency achieved via the *in situ* synthesis allows for more consistency in the presence of Ag NP within the nanogels compared to the synthesis using purchased Ag NPs. A homogenous

and consistent loading of Ag NPs within nanogels is crucial for their application in a clinical setting. Due to this and the removal of the need to purchase or synthesize Ag NPs, the *in situ* synthesis may prove a better synthesis to pursue for this project. However, given size is a key parameter in the toxicity and behavior of Ag NPs *in vivo* [95,100], further characterization of the size and dispersity of the Ag NPs formed is needed. Importantly, optimization to the degree of methacrylation of the pre-polymer and to the crosslinking parameters must be performed to increase the stability of the nanogels if they are to be applicable in a clinical setting.

The synthesis of Ag NP loaded nanogels with purchased Ag NPs was successful. TEM image analysis reported nanogels to be 80 ± 25 nm, with loaded Ag NPs sized at 5 ± 1 nm. Low loading levels were seen in the nanogels, with analysis of TEM images estimating 2 ± 1 Ag NPs per nanogel. DLS measurements stated a hydrodynamic diameter of 123 ± 2 nm in hexanes, falling within the ideal size range for passive accumulation within the tumor [34]. However, the nanogels would likely fall outside the desired size range within an aqueous environment. The PDIs reported by the DLS were all < 0.1, with the sample average being 0.06 and indicating a low polydispersity. The dispersity of the loaded nanogels compare favorably with PDIs reported in the literature for other nanogels synthesized using microfluidics [85,98]. The stability of the nanogels was examined by DLS measurement 44 days post synthesis and reported a hydrodynamic diameter of 134 ± 6 nm with an average PDI of 0.09. Indicating a slight increase of size and polydispersity over the time-period but remaining with a low-polydispersity and within the desired size range. Release experiments conducted in DI water at both pH 5-6 and 6-7, provide support for the release of Ag NPs from the nanogels in an acidic environment. The presence of a second DLS peak in the later measurements indicated the appearance of a particle population smaller than that of the nanogels

present (82 ± 15, 61 ± 8, 151 ± 7 nm). The discrepancy between the hydrodynamic diameter of the secondary peaks and that of the Ag NPs during characterization can be attributed to residual nanogel attached to the Ag NPs after erosion, the aggregation of Ag NPs in the acidic environment or a combination of both. The secondary peak could also be attributed to an artifact of the auto correlation used by the DLS equipment.

Future work on this project must focus on a more extensive characterization of the release of Ag NPs from the nanogels in an acidic environment. Specifically, DLS experiments should be used to decern the time dependence of the release, as this will be critical to the system's biomedical application. Certain SDDSs may ideally require a sustained and long-term release of therapeutic agents over the course of days/weeks. This system would be best suited to a quicker burst release to ensure the dose of Ag NPs is released and diffused into the tumor in the time frame between administering the SDDS and the radiation therapy. Future work should also examine the specific pH at which release begins, to ensure release will not begin within the pH of healthy tissues. The potential or amount of Ag NP aggregation in the acidic environment must also be determined as that will impede both diffusion of the Ag NPs throughout the tumor and their effectiveness as radiosensitizers. Additionally, TEM experiments should also be performed to confirm the release of the Ag NPs. TEM grids should be loaded with nanogel samples at different pH levels, as well as at different times of exposure for each pH level. TEM should allow the visualization of Ag NPs inside nanogels at neutral pH levels and then outside the nanogels at an acidic pH. It should also allow the visualization of decreasing levels of Ag NPs within nanogels over time, depending on the time scale of the release. To optimize passive accumulation within the tumor due to the EPR effect the size of the nanogels should be reduced in order to fall within the required size range in

an aqueous medium. Use of the reported methodology to produce nanogels loaded with different cargo (Au NPs, or chemotherapeutics), is another area of exploration for future work as it will elucidate the extent of tunability made available by the system.

Cell experiments will be a crucial next step for determining the viability of this system. Future studies must explore the impact of the loaded nanogel system on the viability of cells. The extent of cellular uptake of the Ag NPs should be evaluated through dissolution of cells after a period of uptake, and determination of Ag concentration present within cells via mass spectrometry. Additionally visual characterization of cellular uptake should be explored using darkfield imaging, or TEM imaging of cryogenically frozen and sliced cells. Determining the impact of Ag NP aggregation, or residual nanogel present on Ag NPs on the cellular uptake will also be of importance. Cellular experiments will also be needed to confirm that the concentration of Ag NPs that is delivery by system produces the desired level of enhancement to RT results. Future studies should also aim to determine the cytotoxic impact of the Ag NPs in this system on cells without the stimulation of RT, so the potential for unintended cytotoxic effects can be evaluated. Cell experiments should also be used to determine the time scale of erosion of the nanogels as the presence of cellular enzymes should facilitate the degradation of the system.

This work adds to the important body of literature exploring the use of microfluidic devices for the synthesis of nano-scale systems [25,84,85]. Microfluidic devices use reagents more efficiently and provide a potential for scalability that is not present in traditional bulk synthesis methods but needed for the translation to use in a clinical setting [25]. SDDSs provide a unique opportunity to reduce the devastating side effects associated with the most commonly used cancer treatments such as radiation therapy. The development of scalable, simple and tunable methods for the

fabrication of SDDSs is then imperative for the systems to be applicable for clinical use. The results of this thesis support the literature findings that microfluidic devices produce low polydispersity (PDI < 0.1) nano-scale SDDSs in a relatively simplistic process. The fabrication of loaded nanogels through the use of either pre-synthesized Ag NPs or by the *in situ* synthesis of Ag NPs from $AgNO_3$ preformed in this thesis supports the tuneability of the system to different uses.

References

1. Ferlay, J. *et al.* Cancer statistics for the year 2020: An overview. *Int J Cancer* **149**, 778–789 (2021).
2. Brenner, D. R. *et al.* Projected estimates of cancer in Canada in 2022. *CMAJ* **194**, E601–E607 (2022).
3. Ellison, L. F. Health Reports The cancer survival index: Measuring progress in cancer survival to help evaluate cancer control efforts in Canada. doi:10.25318/82003x202100900002eng.
4. Canadian Cancer Society & Canadian Cancer Society's Advisory Committee on Cancer Statistics. *Canadian Cancer Statistics 2017*. *Canadian Cancer Society* vol. 2017 (2017).
5. Garaszczuk, R., Yong, J. H. E., Sun, Z. & de Oliveira, C. The Economic Burden of Cancer in Canada from a Societal Perspective. *Current Oncology* **29**, 2735–2748 (2022).
6. McGranahan, N. & Swanton, C. Biological and therapeutic impact of intratumor heterogeneity in cancer evolution. *Cancer Cell* **27**, 15–26 (2015).
7. Burrell, R. A., McGranahan, N., Bartek, J. & Swanton, C. The causes and consequences of genetic heterogeneity in cancer evolution. *Nature* **501**, 338–345 (2013).
8. Reiter, J. G. *et al.* An analysis of genetic heterogeneity in untreated cancers. *Nat Rev Cancer* **19**, 639–650 (2019).
9. McGranahan, N. & Swanton, C. Clonal Heterogeneity and Tumor Evolution: Past, Present, and the Future. *Cell* **168**, 613–628 (2017).
10. Cheng, M. *et al.* Modern radiation further improves survival in non-small cell lung cancer: An analysis of 288,670 patients. *J Cancer* **10**, 168–177 (2019).
11. Tonse, R. *et al.* Hospitalization rates from radiotherapy complications in the United States. *Sci Rep* **12**, (2022).
12. McKinnell, R. G., Parchment, R. E., Perantoni, A. O., Pierce, G. B. & Damjanov, I. The Biological Basis of Cancer. *The Biological Basis of Cancer* (2006) doi:10.1017/CBO9780511816642.
13. Her, S., Jaffray, D. A. & Allen, C. Gold nanoparticles for applications in cancer radiotherapy: Mechanisms and recent advancements. *Adv Drug Deliv Rev* **109**, 84–101 (2017).
14. Baskar, R., Lee, K. A., Yeo, R. & Yeoh, K. W. Cancer and radiation therapy: Current advances and future directions. *International Journal of Medical Sciences* vol. 9 193–199 Preprint at https://doi.org/10.7150/ijms.3635 (2012).
15. McKinnell, R., Parchment, R., Perantoni, A., Pierce, G., & Damjanov, I. *The Biological Basis of Cancer*. *Corneal Graft Failure* (2006). doi:https://doi.org/10.1017/CBO9780511816642.

16. Rosa, S., Connolly, C., Schettino, G., Butterworth, K. T. & Prise, K. M. Biological mechanisms of gold nanoparticle radiosensitization. *Cancer Nanotechnology 2017 8:1* **8**, 1–25 (2017).
17. Bromma, K. & Chithrani, D. B. Advances in Gold Nanoparticle-Based Combined Cancer Therapy. *Nanomaterials 2020, Vol. 10, Page 1671* **10**, 1671 (2020).
18. Miranda, R. R., Sampaio, I. & Zucolotto, V. Exploring silver nanoparticles for cancer therapy and diagnosis. *Colloids Surf B Biointerfaces* **210**, 112254 (2022).
19. Khan, M. I. *et al.* Recent Progress in Nanostructured Smart Drug Delivery Systems for Cancer Therapy: A Review. *ACS Applied Bio Materials* vol. 5 971–1012 Preprint at https://doi.org/10.1021/acsabm.2c00002 (2022).
20. Clasky, A. J., Watchorn, J. D., Chen, P. Z. & Gu, F. X. From prevention to diagnosis and treatment: Biomedical applications of metal nanoparticle-hydrogel composites. *Acta Biomater* **122**, 1–25 (2021).
21. Ismail, H., Irani, M. & Ahmad, Z. Starch-Based Hydrogels: Present Status and Applications. (2013) doi:10.1080/00914037.2012.719141.
22. Vigata, M., Meinert, C., Pahoff, S., Bock, N. & Hutmacher, D. W. Gelatin methacryloyl hydrogels control the localized delivery of albumin-bound paclitaxel. *Polymers (Basel)* **12**, (2020).
23. Yue, K. *et al.* Synthesis, properties, and biomedical applications of gelatin methacryloyl (GelMA) hydrogels. *Biomaterials* **73**, 254–271 (2015).
24. Chamkouri, H. A Review of Hydrogels, Their Properties and Applications in Medicine. *Am J Biomed Sci Res* **11**, 485–493 (2021).
25. Mauri, E., Giannitelli, S. M., Trombetta, M. & Rainer, A. Synthesis of Nanogels: Current Trends and Future Outlook. *Gels 2021, Vol. 7, Page 36* **7**, 36 (2021).
26. Hanahan, D. & Weinberg, R. A. Hallmarks of Cancer: The Next Generation. *Cell* **144**, 646–674 (2011).
27. Smyth, M. J., Hayakawa, Y., Takeda, K. & Yagita, H. NEW ASPECTS OF NATURAL-KILLER- CELL SURVEILLANCE AND THERAPY OF CANCER. *Nature Reviews* **2**, 850–861 (2002).
28. Alberts, B. *et al.* Programmed Cell Death (Apoptosis). (2002).
29. Hayflick, L. & Moorhead, P. S. *THE SERIAL CULTIVATION OF HUMAN DIPLOID CELL STRAINS'*. *Experimental Cell Research* vol. 25 (1961).
30. Trédan, O., Galmarini, C. M., Patel, K. & Tannock, I. F. Drug resistance and the solid tumor microenvironment. *J Natl Cancer Inst* **99**, 1441–1454 (2007).
31. Valente, K. P. *et al.* Microfluidic technologies for anticancer drug studies. *Drug Discov Today* **22**, 1654–1670 (2017).
32. Semenza, G. L. HIF-1 and tumor progression: pathophysiology and therapeutics. *Trends Mol Med* **8**, S62–S67 (2002).
33. Carmeliet, P. & Jain, R. K. Molecular mechanisms and clinical applications of angiogenesis. *Nature* **473**, 298–307 (2011).

34. Kang, M. G. *et al.* Nanogels Derived from Fish Gelatin: Application to Drug Delivery System. *Mar Drugs* **17**, (2019).
35. Li, Z., Huang, J. & Wu, J. pH-Sensitive nanogels for drug delivery in cancer therapy. *Biomater Sci* **9**, 574–589 (2021).
36. Bazak, R., Houri, M., El Achy, S., Kamel, S. & Refaat, T. Cancer active targeting by nanoparticles: a comprehensive review of literature. *J Cancer Res Clin Oncol* **141**, 769–784 (2015).
37. Mi, P. Stimuli-responsive nanocarriers for drug delivery, tumor imaging, therapy and theranostics. *Theranostics* **10**, 4557–4588 (2020).
38. Piao, Y. *et al.* Biomedical applications of gelatin methacryloyl hydrogels. *Engineered Regeneration* vol. 2 47–56 Preprint at https://doi.org/10.1016/j.engreg.2021.03.002 (2021).
39. Hossen, S. *et al.* Smart nanocarrier-based drug delivery systems for cancer therapy and toxicity studies: A review. *J Adv Res* **15**, 1–18 (2019).
40. Dong, Z. *et al.* CaCO3 nanoparticles as an ultra-sensitive tumor-pH-responsive nanoplatform enabling real-time drug release monitoring and cancer combination therapy. *Biomaterials* **110**, 60–70 (2016).
41. Haume, K. *et al.* Gold nanoparticles for cancer radiotherapy: a review. *Cancer Nanotechnology* vol. 7 Preprint at https://doi.org/10.1186/s12645-016-0021-x (2016).
42. Alhussan, A., Bozdoğan, E. P. D. & Chithrani, D. B. Combining Gold Nanoparticles with Other Radiosensitizing Agents for Unlocking the Full Potential of Cancer Radiotherapy. *Pharmaceutics 2021, Vol. 13, Page 442* **13**, 442 (2021).
43. Liu, P. *et al.* Silver nanoparticles outperform gold nanoparticles in radiosensitizing U251 cells in vitro and in an intracranial mouse model of glioma. *Int J Nanomedicine* **11**, 5003–5014 (2016).
44. Butterworth, K. T., McMahon, S. J., Currell, F. J. & Prise, K. M. Physical basis and biological mechanisms of gold nanoparticle radiosensitization. *Nanoscale* **4**, 4830–4838 (2012).
45. Schuemann, J. *et al.* Roadmap to Clinical Use of Gold Nanoparticles for Radiation Sensitization. *International Journal of Radiation Oncology*Biology*Physics* **94**, 189–205 (2016).
46. Hainfeld, J. F., Slatkin, D. N. & Smilowitz, H. M. The use of gold nanoparticles to enhance radiotherapy in mice. *Phys Med Biol* **49**, N309 (2004).
47. Liu, P. *et al.* Silver nanoparticles: A novel radiation sensitizer for glioma? *Nanoscale* **5**, 11829–11836 (2013).
48. Liu, Z. *et al.* Enhancement of radiotherapy efficacy by silver nanoparticles in hypoxic glioma cells. *Artif Cells Nanomed Biotechnol* **46**, S922–S930 (2018).
49. Paul, A. *et al.* Injectable Graphene Oxide/ Hydrogel-Based Angiogenic Gene Delivery System for Vasculogenesis and Cardiac Repair. (2014) doi:10.1021/nn5020787.

50. Chang, H. *et al.* CommuniCation 1702243 (1 of 8) A Swellable Microneedle Patch to Rapidly Extract Skin Interstitial Fluid for Timely Metabolic Analysis. (2017) doi:10.1002/adma.201702243.
51. Ryon Shin, S. *et al.* Reduced Graphene Oxide-GelMA Hybrid Hydrogels as Scaffolds for Cardiac Tissue Engineering. *Small* **12**, 3677–3689 (2016).
52. Levett, P. A. *et al.* A biomimetic extracellular matrix for cartilage tissue engineering centered on photocurable gelatin, hyaluronic acid and chondroitin sulfate. (2013) doi:10.1016/j.actbio.2013.10.005.
53. Journal, A. I., Modaresifar, K., Hadjizadeh, A. & Niknejad, H. Artificial Cells, Nanomedicine, and Biotechnology Design and fabrication of GelMA/chitosan nanoparticles composite hydrogel for angiogenic growth factor delivery. (2017) doi:10.1080/21691401.2017.1392970.
54. Byambaa, B. *et al.* Bioprinted Osteogenic and Vasculogenic Patterns for Engineering 3D Bone Tissue. (2017) doi:10.1002/adhm.201700015.
55. Peppas, N. A., Hilt, J. Z., Khademhosseini, A. & Langer, R. Hydrogels in biology and medicine: From molecular principles to bionanotechnology. *Advanced Materials* **18**, 1345–1360 (2006).
56. Pereira, R. F. & Bártolo, P. J. 3D Photo-Fabrication for Tissue Engineering and Drug Delivery 3D Printing-Review. *www.engineering.org.cn Engineering* **1**, 90–112 (2015).
57. Billiet, T., Gevaert, E., De Schryver, T., Cornelissen, M. & Dubruel, P. The 3D printing of gelatin methacrylamide cell-laden tissue-engineered constructs with high cell viability. *Biomaterials* **35**, 49–62 (2014).
58. Reithofer, M. R., Lakshmanan, A., Ping, A. T. K., Chin, J. M. & Hauser, C. A. E. In situ synthesis of size-controlled, stable silver nanoparticles within ultrashort peptide hydrogels and their anti-bacterial properties. *Biomaterials* **35**, 7535–7542 (2014).
59. Chen, Y.-C. *et al.* Functional Human Vascular Network Generated in Photocrosslinkable Gelatin Methacrylate Hydrogels. *Adv. Funct. Mater* **22**, 2027–2039 (2012).
60. Young, A. T. *et al.* Rheological Properties of Coordinated Physical Gelation and Chemical Crosslinking in Gelatin Methacryloyl (GelMA) Hydrogels. *Macromol Biosci* **20**, 2000183 (2020).
61. Gholamali, I. & Yadollahi, M. Bio-nanocomposite Polymer Hydrogels Containing Nanoparticles for Drug Delivery: a Review. *Regen Eng Transl Med* **7**, 129–146 (2021).
62. Van Den Bulcke, A. I. *et al.* Structural and Rheological Properties of Methacrylamide Modified Gelatin Hydrogels. (2000) doi:10.1021/bm990017d.
63. Bupphathong, S. *et al.* Gelatin Methacrylate Hydrogel for Tissue Engineering Applications;A Review on Material Modifications. *Pharmaceuticals 2022, Vol. 15, Page 171* **15**, 171 (2022).
64. Van Vlierberghe, S., Dubruel, P. & Schacht, E. Effect of Cryogenic Treatment on the Rheological Properties of Gelatin Hydrogels. doi:10.1177/0883911510377254.

65. Pepelanova, I., Kruppa, K., Scheper, T. & Lavrentieva, A. Gelatin-Methacryloyl (GelMA) Hydrogels with Defined Degree of Functionalization as a Versatile Toolkit for 3D Cell Culture and Extrusion Bioprinting. *Bioengineering (Basel)* **5**, (2018).
66. Choi, J. R., Yong, K. W., Choi, J. Y. & Cowie, A. C. Recent advances in photo-crosslinkable hydrogels for biomedical applications. *https://doi.org/10.2144/btn-2018-0083* **66**, 40–53 (2019).
67. Nguyen, K. T. & West, J. L. Photopolymerizable hydrogels for tissue engineering applications. *Biomaterials* **23**, 4307–4314 (2002).
68. Rouillard, A. D. *et al.* Methods for Photocrosslinking Alginate Hydrogel Scaffolds with High Cell Viability. *https://home.liebertpub.com/tec* **17**, 173–179 (2010).
69. Qin, X. H., Ovsianikov, A., Stampfl, J. & Liska, R. Additive manufacturing of photosensitive Hydrogels for tissue engineering applications. *BioNanoMaterials* **15**, 49–70 (2014).
70. Williams, C. G., Malik, A. N., Kim, T. K., Manson, P. N. & Elisseeff, J. H. Variable cytocompatibility of six cell lines with photoinitiators used for polymerizing hydrogels and cell encapsulation. *Biomaterials* **26**, 1211–1218 (2005).
71. Bryant, S. J., Nuttelman, C. R. & Anseth, K. S. Cytocompatibility of UV and visible light photoinitiating systems on cultured NIH/3T3 fibroblasts in vitro. doi:10.1163/156856200743805.
72. Fairbanks, B. D., Schwartz, M. P., Bowman, C. N. & Anseth, K. S. Photoinitiated polymerization of PEG-diacrylate with lithium phenyl-2,4,6-trimethylbenzoylphosphinate: polymerization rate and cytocompatibility. *Biomaterials* **30**, 6702–6707 (2009).
73. Nguyen, T.-U., Watkins, K. E. & Kishore, V. Photochemically crosslinked cell-laden methacrylated collagen hydrogels with high cell viability and functionality. (2019) doi:10.1002/jbm.a.36668.
74. Xu, H., Casillas, J., Krishnamoorthy, S. & Xu, C. Effects of Irgacure 2959 and lithium phenyl-2,4,6-trimethylbenzoylphosphinate on cell viability, physical properties, and microstructure in 3D bioprinting of vascular-like constructs. *Biomedical Materials (Bristol)* **15**, (2020).
75. Sabnis, A., Rahimi, M., Chapman, C. & Nguyen, K. T. Cytocompatibility studies of an in situ photopolymerized thermoresponsive hydrogel nanoparticle system using human aortic smooth muscle cells. (2008) doi:10.1002/jbm.a.32194.
76. Elkhoury, K., Zuazola, J. & Vijayavenkataraman, S. Bioprinting the future using light: A review on photocrosslinking reactions, photoreactive groups, and photoinitiators. *SLAS Technol* (2023) doi:10.1016/J.SLAST.2023.02.003.
77. Majima, E. *et al.* Phenyl-2,4,6-trimethylbenzoylphosphinates as water-soluble photoinitiators . Generation and reactivity of O = b (C6Hs)(O-) radical anions. **2315**, 2307–2315 (1991).

78. Kaur, M., Sudhakar, K. & Mishra, V. Fabrication and biomedical potential of nanogels: An overview. *International Journal of Polymeric Materials and Polymeric Biomaterials* **68**, 287–296 (2019).
79. Kousalová, J. & Etrych, T. Polymeric Nanogels as Drug Delivery Systems. *Physiol. Res* **67**, 305–317 (2018).
80. Soni, K. S., Desale, S. S. & Bronich, T. K. Nanogels: An overview of properties, biomedical applications and obstacles to clinical translation. (2015) doi:10.1016/j.jconrel.2015.11.009.
81. Yang, G., Wang, X., Fu, S., Tang, R. & Wang, J. pH-triggered chitosan nanogels via an ortho ester-based linkage for efficient chemotherapy. *Acta Biomater* **60**, 232–243 (2017).
82. Sahu, P. *et al.* pH responsive biodegradable nanogels for sustained release of bleomycin. *Bioorg Med Chem* **25**, 4595–4613 (2017).
83. Li, C., Obireddy, S. R. & Lai, W. F. Preparation and use of nanogels as carriers of drugs. *Drug Deliv* **28**, 1594–1602 (2021).
84. Chiesa, E. *et al.* The microfluidic technique and the manufacturing of polysaccharide nanoparticles. *Pharmaceutics* **10**, (2018).
85. Mahmoudi, Z. *et al.* Promoted chondrogenesis of hMCSs with controlled release of TGF-β3 via microfluidics synthesized alginate nanogels. (2019) doi:10.1016/j.carbpol.2019.115551.
86. Ni, Y., Zhao, L., Xue, X., Guoying, X. & Zhao, C. Research progress of hydrogel-mediated disease therapeutics. *Journal of Nanoparticle Research* **23**, 105 (2021).
87. Zhao, C.-X. & Middelberg, A. P. J. Synthesis and Characterization of Nanomaterials Using Microfluidic Technology. in *Handbook of Nanoparticles* 1–16 (Springer International Publishing, 2015). doi:10.1007/978-3-319-13188-7_23-1.
88. Valente, K. P. The Applications of Microfluidic Platforms for Cancer Research: The Tumor Microenvironment and Drug Delivery Systems. (University of Victoria, 2020).
89. Zhao, D. H. *et al.* An in situ synthesis of silver nanoparticle-loaded genetically engineered polypeptide nanogels for antibacterial and wound healing applications. *Dalton Transactions* **49**, 12049–12055 (2020).
90. Zhang, B. J., Xu, S. & Kumacheva, E. Photogeneration of Fluorescent Silver Nanoclusters in Polymer Microgels **. *Advanced Materi* **17**, 2336–2340 (2005).
91. Xu, R. *et al.* Ag nanoparticles sensitize IR-induced killing of cancer cells. *Cell Research 2009 19:8* **19**, 1031–1034 (2009).
92. Sun, M. *et al.* Synthesis and properties of gelatin methacryloyl (GelMA) hydrogels and their recent applications in load-bearing tissue. *Polymers (Basel)* **10**, (2018).
93. Stetefeld, J., McKenna, S. A. & Patel, T. R. Dynamic light scattering: a practical guide and applications in biomedical sciences. *Biophys Rev* **8**, 409–427 (2016).
94. Khan, I., Saeed, K. & Khan, I. Nanoparticles: Properties, applications and toxicities. *Arabian Journal of Chemistry* **12**, 908–931 (2019).

95. De Leersnyder, I., De Gelder, L., Van Driessche, I. & Vermeir, P. Revealing the importance of aging, environment, size and stabilization mechanisms on the stability of metal nanoparticles: A case study for silver nanoparticles in a minimally defined and complex undefined bacterial growth medium. *Nanomaterials* **9**, (2019).
96. Agnihotri, S., Mukherji, S. & Mukherji, S. Size-controlled silver nanoparticles synthesized over the range 5–100 nm using the same protocol and their antibacterial efficacy. *RSC Adv* **4**, 3974–3983 (2013).
97. Gorham, J. M., MacCuspie, R. I., Klein, K. L., Fairbrother, D. H. & Holbrook, D. UV-induced photochemical transformations of citrate-capped silver nanoparticle suspensions. *Journal of Nanoparticle Research* **14**, (2012).
98. Huang, K. *et al.* Small, Traceable, Endosome-Disrupting, and Bioresponsive Click Nanogels Fabricated via Microfluidics for CD44-Targeted Cytoplasmic Delivery of Therapeutic Proteins. *ACS Appl Mater Interfaces* **11**, 22171–22180 (2019).
99. Bromma, K., Bannister, A., Kowalewski, A., Cicon, L. & Chithrani, D. B. Elucidating the fate of nanoparticles among key cell components of the tumor microenvironment for promoting cancer nanotechnology. *Cancer Nanotechnology 2020 11:1* **11**, 1–16 (2020).
100. Bélteky, P. *et al.* Are smaller nanoparticles always better? Understanding the biological effect of size-dependent silver nanoparticle aggregation under biorelevant conditions. *Int J Nanomedicine* **16**, 3021–3040 (2021).